NASA Technical Paper 3455

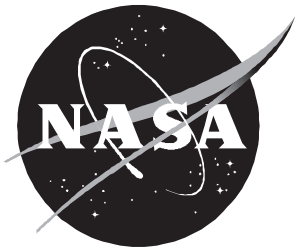

Active Load Control During Rolling Maneuvers

Jessica A. Woods-Vedeler, Anthony S. Pototzky, and Sherwood T. Hoadley

October 1994

NASA Technical Paper 3455

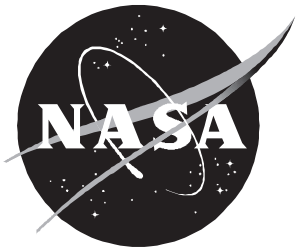

Active Load Control During Rolling Maneuvers

Jessica A. Woods-Vedeler
Langley Research Center • Hampton, Virginia

Anthony S. Pototzky
Lockheed Engineering & Sciences Company • Hampton, Virginia

Sherwood T. Hoadley
Langley Research Center • Hampton, Virginia

National Aeronautics and Space Administration
Langley Research Center • Hampton, Virginia 23681-0001

October 1994

The use of trademarks or names of manufacturers in this report is for accurate reporting and does not constitute an official endorsement, either expressed or implied, of such products or manufacturers by the National Aeronautics and Space Administration.

This publication is available from the following sources:

NASA Center for AeroSpace Information
800 Elkridge Landing Road
Linthicum Heights, MD 21090-2934
(301) 621-0390

National Technical Information Service (NTIS)
5285 Port Royal Road
Springfield, VA 22161-2171
(703) 487-4650

Contents

Abstract 1

Introduction 1

Symbols and Abbreviations 2

RMLA Design Concept 5

Active Flexible Wing Program 5

- Background 5
- Wind Tunnel Model 6
  - Construction 6
  - Control surfaces 6
  - Instrumentation 7
  - Tip ballast stores 7
  - Sting mount 7
- Digital Controller 7

Plant Equations 8

- Plant Equations of Motion 8
  - Nonlinear model 9
  - Linear model 9
- Effect of Pendulum Term on Plant Equations of Motion 10
- Design-Model Equations of Motion 10
- Plant Output Equations 10

RMLA Control Law Synthesis 11

- Synthesis Procedure 12
- Synthesis Steps 12
  - Evaluate control surface load effectiveness 13
  - Determine potential control law form 13
  - Determine control law gains 14
  - Determine control system stability and robustness 15

Wind Tunnel, Test Procedures, and Data Reduction for RMLA Performance Evaluation 16

- Wind Tunnel 16
- Test Procedures 16
- Data Reduction for RMLA Performance Evaluation 17

Results and Discussion 18

- Experimental Results 18
  - Time history comparisons of incremental loads 18
  - Typical load alleviation results 19
  - Overall analysis of experimental results 19
  - Summary of experimental results 21
- Comparison of Experimental and Analytical Results 21
- Multiple-Function Control Law Performance Results 21

Concluding Remarks 22

Appendix A—Aeroelastic Analysis and Parameter Identification 24
Appendix B—Calculation of Mass Eccentricity Effects 28
References 30
Tables 31
Figures 37

Abstract

A rolling maneuver load alleviation (RMLA) system has been demonstrated on the Active Flexible Wing (AFW) wind tunnel model in the Langley Transonic Dynamics Tunnel (TDT). The objective was to develop a systematic approach for designing active control laws to alleviate wing loads during rolling maneuvers. Two RMLA control laws were developed that utilized outboard control-surface pairs (leading and trailing edge) to counteract the loads and that used inboard trailing-edge control-surface pairs to maintain roll performance. Rolling maneuver load tests were performed in the TDT at several dynamic pressures that included two below and one 11 percent above the open-loop flutter dynamic pressure. The RMLA system was operated simultaneously with an active flutter suppression system above open-loop flutter dynamic pressure. At all dynamic pressures for which baseline results were obtained, torsion-moment loads were reduced for both RMLA control laws. Results for bending-moment load reductions were mixed; however, design equations developed in this study provided conservative estimates of load reduction in all cases.

Introduction

Without the use of active control laws, passive solutions must be provided to suppress unfavorable aeroelastic response. These solutions result in increased structural stiffness of the wing; and thus, in increased weight. In the past 20 years, the use of active controls has been investigated extensively as a means to control the aeroelastic response of aircraft. Gust load alleviation by using active control laws has been successfully implemented on aircraft such as the Lockheed L.1011 (ref. 1) and the Airbus A320 (ref. 2). Flutter suppression has been demonstrated through wind tunnel tests of a variety of aircraft (refs. 3 and 4) and validated in flight tests on such aircraft as the B-52 (ref. 5) and the F-4F (ref. 6). Until recently, however, the use of active control laws has not been successfully developed to alleviate wing loads generated during rolling maneuvers. Consequently, aircraft wings are still designed to support the increased loads generated during rolling maneuvers through added structural stiffness. The resultant increase in wing weight may be unnecessary if active control law technology was available to alleviate loads. Some past research has indicated the feasibility of using active control laws for rolling maneuver load alleviation.

During early tests of the Active Flexible Wing (AFW), maneuver load control systems were demonstrated for longitudinal motion (ref. 7). The concepts reduce wing-root bending moment during pitch maneuvers through the use of angle-of-attack feedback, scheduled wing cambering by control surface deflections, and bending-moment strain gauge feedback. Significant reductions in bending moment were achieved. Because of this success, the possibility of designing a control law to actively reduce wing loads during rolling maneuvers was considered feasible. During this test, an active roll control system (ARC) was developed to maneuver the model to a commanded roll angle position at a specified roll rate. While evaluating this control law, the potential for using active controls to redistribute wing loads during rolling maneuvers was recognized; however, a systematic approach for designing these control laws was not developed.

The intent of the current research was to develop rolling maneuver load alleviation (RMLA) control laws that would reduce dynamic wing loads with digital active controls during fast rolling maneuvers. In this paper, a systematic synthesis approach that involves three steps is defined for developing RMLA control laws. The first step analytically evaluated the ability of each

control surface to affect loads during fast rolling maneuvers and required developing analytical evaluation procedures. The next step established effective control surface combinations and a feedback control law form that could potentially reduce dynamic loads. The third step iterated control system gains for the various control surface combinations to determine a set of gains that effectively reduces dynamic loads during specified rolling maneuvers while maintaining adequate stability margins. With this approach, two RMLA control laws, which differ in selection of control surface pairs, were developed for the AFW wind tunnel model shown in figures 1(a) and 1(b). These two control laws were experimentally evaluated by performing controlled rolling maneuvers of the AFW wind tunnel model in the Langley Transonic Dynamics Tunnel (TDT). Experimental load alleviation results are presented in this paper and compared with analytically predicted load reductions from an experimentally determined plant model. Results from rolling maneuvers performed at dynamic pressures above the open-loop flutter boundary in which a flutter suppression control law was operating in conjunction with an RMLA control law are also presented. Appendix A explains the development of the experimentally determined plant model equations. Appendix B provides the details of a study conducted to determine the effect of mass eccentricity on the plant model.

Symbols and Abbreviations

$\mathbf{A}$	state-space form system coefficient matrix
AD	analog to digital
AFW	Active Flexible Wing
AP	array processor
ARC	active roll control
$\mathbf{B}$	state-space form control coefficient matrix
$\mathbf{B}_e$	matrix representing coefficient of nonlinear pendulum term
BMI	bending moment inside
BMO	bending moment outside
b	reference wing span
$\mathbf{C}$	state-space form output system coefficient matrix
c.g.	center of gravity
$\mathbf{D}$	state-space form output control coefficient matrix
DA	digital to analog
DCS	digital controller system
DOF	degrees of freedom
DSP	digital signal processor
$\mathbf{E}$	steady-state load
$\mathbf{F}$	controller state matrix
FSS	flutter suppression system
$\mathbf{G}$	controller transfer matrix
g	acceleration due to gravity, in/sec^2
G_1, G_2, G_3	load effectiveness control system gains

$\mathbf{H}$	plant transfer matrix
$\mathbf{I}$	identity matrix
I_{xx}	roll moment of inertia (256.872 in-lb-sec^2)
$K_{\mathrm{com}}, K_{\mathrm{TEI}}, K_{\mathrm{TEO}}, K_{\mathrm{LEO}}$	control system feedback gains
k_n	gain margin
L	rolling moment
$\mathbf{L}$	diagonal gain and phase change matrix
L_p	rolling moment due to roll rate, in-lb-sec
L_{δ_i}	rolling moment due to deflection of control surface i
LEO	leading-edge outboard
l	distance between model c.g. and roll axis, in.
ℓ	index
M	moment, in-lb
$\mathcal{M}_m$	integral over time of pendulum contribution to total rolling moment
$\mathcal{M}_\delta$	integral over time of control surface contribution to total rolling moment
m	model mass, lb-sec^2/in.
max	maximum
q	dynamic pressure, lb/ft^2
RMLA	rolling maneuver load alleviation
RRTS	roll rate tracking system
RTS	roll-trim system
RVDT	resistance variable distance transducer
S	wing area
s	Laplace variable
T_δ	transfer function
TDT	Langley Transonic Dynamics Tunnel
TEI	trailing-edge inboard
TEO	trailing-edge outboard
TMI	torsion moment inboard
TMO	torsion moment outboard
t	time
t_F	time to maneuver through 90°, sec
$\mathbf{u}$	input vector
u_e	nonlinear pendulum variable, sin ϕ

V	free-stream velocity
$\mathbf{x}, \dot{\mathbf{x}}$	vector of state variables and its time derivative
$\mathbf{y}$	output vector
$\mathbf{z}$	sensor output
δ	control surface deflection, deg
$\overline{\sigma}$	maximum singular value
$\phi, \dot{\phi}, \ddot{\phi}$	roll angle and its time derivatives
ω	frequency, rad/sec
Subscripts:	
b	bending
c	control
com	command
f	feedback
I	inboard
i	control surface index
L	left wing
L	peak, or limiting, value
l	linearized
ℓ	index
Load	parameter identification load
m	mass
min	minimum
O	outboard
p	roll rate
R	right wing
ss	steady state at 90° (roll brake off condition)
t	torsion
t_B	break time after which command held constant
t_F	time to maneuver through 90°
δ	control surface
0°	steady state at 0° (roll brake off condition)
90°	steady state at 90° (roll brake off condition)
Superscript:	
T	matrix transpose

RMLA Design Concept

The objective of the research presented in this paper was to develop an active RMLA control laws design that would attempt to alleviate both bending-moment and torsion-moment wing loads during fast rolling maneuvers. Specifically, the concept reported herein involves designing control laws that minimize the peak deviation from the steady-state value of the wing loads during a rolling maneuver. Partial motivation for choosing the peak deviation from the steady-state value as basis of load reduction was the large artificially induced static loads that result from the model being constrained to roll about a sting in the wind tunnel. This would not occur to an aircraft in flight. The basis for RMLA design in that case could be, for example, the loads about the load point induced by gravity. However, the systematic synthesis approach defined in this paper for developing RMLA control laws would be the same.

The deviation of a load from its steady-state value is referred to as an incremental load and is illustrated in figure 2. The actual load during a rolling maneuver is shown in figure 2(a) as a function of time. The steady-state load, which is defined to be the load at the beginning of the maneuver, and the incremental load, defined to be the difference between the actual load and the steady-state load, are shown. Figure 2(b) shows the magnitude of the incremental load as a function of time. The dot in the figure indicates the maximum absolute deviation defined herein as the peak incremental load. It is the peak incremental bending-moment and torsion-moment loads which the RMLA control laws described herein were attempting to reduce. In addition to reducing peak incremental loads, the control laws were designed to meet specified "time-to-roll" performance requirements and certain stability-margin requirements. Also included in the control law design was the requirement that the control laws be implemented by a digital controller. Since discretization of continuous time-domain control laws introduces discretization errors and phase lags, the effect of discretization on control law performance had to be considered in the design.

To evaluate load reduction, it is necessary to compare loads sustained during a rolling maneuver employing an active RMLA control law with those of a baseline rolling maneuver having the same time-to-roll performance. Consequently, a baseline control law had to be designed which met the same time-to-roll performance and stability-margin requirements as the RMLA control laws. The baseline control law, described in this paper, was used to calculate load reductions achieved by each of the RMLA control laws for specific rolling maneuvers.

Active Flexible Wing Program

Background

The AFW was developed at Rockwell International Corporation in the mid-1980's (ref. 7). This concept exploited, rather than avoided, wing flexibility to provide weight savings and improved aerodynamic performance. Weight savings were realized in two ways: (1) a flexible wing and (2) no horizontal tail.

In an AFW wing design, large amounts of aeroelastic twist are permitted to provide improved maneuver aerodynamics at several design points (subsonic, transonic, and supersonic). However, degraded roll performance (in the form of aileron reversal) over a significant portion of the flight envelope is a direct result of large amounts of twist in the wing. In a typical aircraft design, a differential horizontal tail control would be added to provide acceptable roll performance. However, in an AFW design, multiple leading- and trailing-edge wing control surfaces are used in various combinations, up to and beyond reversal, to provide enhanced roll performance.

Additional weight savings can be achieved by the use of active controls to suppress unfavorable aeroelastic responses. Alone or in combination, flutter suppression, gust load alleviation, and

maneuver load alleviation all have the potential for reducing vehicle weight. The payoff for employing an actively controlled AFW would be decreased wing structural weight that would ultimately decrease aircraft gross takeoff weight by 15 percent (refs. 7 and 8).

To demonstrate the AFW, Rockwell International built a wind tunnel model in the mid-1980's that has been evaluated extensively. In cooperation with the USAF and NASA, the AFW model was tested in the Langley Transonic Dynamics Tunnel in 1986 and 1987 to demonstrate the application of digital active-controls technology. In 1989 and 1991, the model, with some modifications to move its flutter boundary into the operating envelope of the TDT, was tested at NASA to further demonstrate aeroelastic control (consistent with the AFW concept) again through the application of digital active-controls technology.

The research documented in this report stems from tests performed during the 1991 evaluation of the AFW wind tunnel model.

Wind Tunnel Model

This section outlines the basic components of the AFW wind tunnel model. The AFW model was a full-span, aeroelastically-scaled representation of a fighter aircraft configuration. Figure 1(a) is a photograph of the model, as configured for the wind tunnel tests in 1989 and 1991. It had a low-aspect ratio wing with a span of approximately 8.67 ft. The model was supported along the wind tunnel test section centerline by a sting mount specifically constructed for this model. This sting utilized an internal ball bearing to allow the model freedom to roll about the sting axis. Figure 1(b) is a multiple-exposure photograph showing the model at four different roll positions. The fuselage was connected to the sting through a pivot so that the model could be remotely pitched from an angle of attack of approximately $-1.5°$ to $13.5°$. Figure 3(a) shows the fuselage skin removed to reveal the model's internal structure and instrumentation. Figure 3(b) shows the basic dimensions of the model, control surfaces, and sting mount. Additional details of the AFW model are included in references 7 and 8.

Construction. The wing of the model is constructed from an aluminum-honeycomb core, cocured with tailored plies of graphite-epoxy composite material. The plies were oriented to permit desired amounts of bending and twist under aerodynamic loads. To provide the airfoil shape without significantly affecting the wing stiffness, the surfaces of graphite-epoxy material were covered by a semirigid polyurethane foam. The rigid fuselage of the model was constructed of aluminum bulkheads and stringers with a fiberglass skin, which was designed to provide a basic aerodynamic shape.

Control surfaces. The shaded areas in figure 3(b) indicate the location of each control surface. There were two leading-edge and two trailing-edge control surfaces on each wing. Each control surface was designed so that the chordwise dimension was 25 percent of the local wing chord and the spanwise dimension was 28 percent of the wing semispan. The control surfaces were constructed of polyurethane foam cores with graphite-epoxy cloth skins.

The control surfaces were connected to the wing by hinge-line-mounted, vane-type rotary actuators powered by an onboard hydraulic system. Deflection limits of $-10°$ to $10°$ were imposed on the control surfaces to avoid exceeding allowable hinge-moment and wing-load limits. Two actuators each were used to drive all of the control surfaces except the outboard, trailing-edge control surfaces, which were each driven by one actuator. As detailed in figure 4, the actuators were connected to the wing structure by cylindrical rods, which were fitted by titanium inserts into the wing. This arrangement was designed to meet shear and torsion requirements placed on the wing-to-control surface connections and to allow for bending freedom of the wing. The contribution of the control surfaces to the wing stiffness was also minimized with this arrangement.

Instrumentation. The AFW wind tunnel model was instrumented with several types of sensors. Strain gauges measured bending and torsion moments and a gyro measured roll rate. Placement of bending- and torsion-moment strain gauges is shown in figure 3 and shown in detail in figure 5. Primary (1) and secondary (2) strain gauges of each type were positioned at four stations located inboard and outboard of each wing. Secondary sensor signals were available if primary sensors failed. The roll-rate gyro was located at an inboard location on the left side of the model as shown in figure 3(a). The model was also instrumented with accelerometers and a roll potentiometer, none of which were used by the RMLA control laws described herein.

Tip ballast stores. Because the model was used to evaluate flutter suppression control laws, the original AFW model was modified before the wind tunnel test in 1989 to move its flutter boundary into the operating envelope of the TDT. This modification consisted of adding a ballast store to each wing tip, as shown in figures 1 and 3. A detailed drawing of the tip store is shown in figure 6. The store was basically a thin, hollow, aluminum tube with internal ballast distributed to lower the wing flutter boundary to a desired dynamic pressure range. Instead of a hard attachment, the store was connected to the wing by a pitch-pivot mechanism. The pivot allowed freedom for the store to pitch relative to the wing surface. When testing for flutter, an internal hydraulic brake held the store to prevent this rotation. This configuration was called the coupled tip-ballast-store configuration. In the event of a flutter instability, this brake was released. In the released or decoupled configuration, the pitch stiffness of the store was provided by an internal spring element, shown in figure 6. The reduced stiffness of the spring element (when compared with the hydraulic brake arrangement) significantly increased the frequency of the first torsion mode of the wing. The change in frequency moved the flutter condition to higher dynamic pressures. This behavior was related to the decoupler pylon as discussed in reference 9. The automatic decoupling of the tip ballasts from the wing structure to rapidly increase the flutter speed of the model during tests in which a flutter instability occurred provided a safety mechanism that prevented damage to the model and the wind tunnel.

Sting mount. The model was supported in the wind tunnel by a sting mount that was constructed expressly for tests of the AFW model. An internal ball bearing allowed the model a roll degree of freedom about the sting and an hydraulic braking system inhibited this degree of freedom. The hydraulic braking system engaged automatically to prevent the umbilical cables running through the sting mount from snapping during rolling maneuvers exceeding 135° or −135°.

Digital Controller

The control laws presented in this document were implemented during wind tunnel tests by using a digital controller system (DCS) (ref. 10). The DCS was a real-time, multiple-function, multi-input/multi-output digital controller developed by NASA as part of the AFW test program. A schematic in figure 7 shows how the system was integrated with the AFW model.

The DCS, as used in the 1991 wind tunnel tests, consisted of a workstation, which housed three separate special purpose processing units: an integer digital signal processor (DSP), a floating-point DSP with two microprocessors, and an array processor (AP). A high-speed integer DSP controlled all the real-time processing including control law execution, data acquisition, and storage. Actual control law computations were performed with the floating-point DSP. High-speed direct memory access for the DCS was provided by the AP. In addition, the AP provided vectorized floating-point processing and served as a backup for the DSP during single-function control law tests.

The DCS was designed to be highly flexible in the structure and the dimension of control laws to be implemented and in the selection of sensors and actuators used. Simultaneous implementation of control laws was possible. A flutter suppression system (FSS) could be tested in conjunction with the roll-trim system (RTS), the roll rate tracking system (RRTS) or the RMLA system.

Additional DCS hardware included two analog-to-digital (AD) converters that transformed up to 64 analog voltage signals from the model instrumentation into digital form and two digital-to-analog (DA) converters that converted up to 16 controller output signals to analog form.

The interface electronics box shown in figure 7 filtered the analog signals being received from the model or sent to the model by the digital controller. The box contained antialiasing filters with either a 25-Hz or 100-Hz break frequency and first- or fourth-order roll-off characteristics. Notch filters were also contained in the box and employed by some FSS control laws to provide additional analog filtering of either input or output signals. The RMLA control laws did not use notch filters, but low pass filters were included analytically.

Plant Equations

The ARC system was designed to minimize control-surface deflections during rolling maneuvers and was experimentally evaluated during the wind tunnel test of the AFW in 1987 (ref. 11). In that study, the frequency of the commanded input was assumed to be well below the frequency of the first flexible mode; consequently, the flexible modes would not be excited by the motion of the control surfaces used by the ARC system for roll control. Only rigid-body motion was used in the design of the ARC system and analytical and experimental results compared well with the previous study. Consequently, the RMLA control laws presented herein used only the rigid-body roll equation and load equations in the design model.

Plant Equations of Motion

The rigid-body roll equation of motion for the open-loop wind tunnel model used in both this study and that of reference 11 is described as follows:

$$I_{xx}\ddot{\phi} - L_p\dot{\phi} + mgl\sin\phi = \sum_{i=1}^{6} L_{\delta_i}\delta_i \tag{1}$$

Many of the coefficients and variables used in the equation are defined in reference 12. However, equation (1) differs in two ways from the equation in reference 12: the control-surface rate derivatives have been neglected and the quantity $mgl\sin\phi$, referred to herein as the pendulum term, has been added. This pendulum term is necessary because the center of gravity of the wind tunnel model is a distance l below the roll axis of the model. This term is not representative of a real aircraft and causes equation (1) to be nonlinear. The nonlinear term can be linearized for small roll angles by the fact that $\sin\phi \approx \phi$ (ϕ in radians); however, for the large roll angles experienced during wind tunnel tests, the small angle assumption is violated. With this approximation, the pendulum term is 57 percent too large at $\phi = 90°$. Nevertheless, this assumption was still considered reasonable to obtain estimates of behavior with a linearized model that includes the pendulum effect. To simplify the design of control laws, a linearized model of the plant was desired. To this end, three sets of plant equations were developed. The first set was composed of linearized state-space equations with the nonlinear pendulum term included explicitly. The second set included a linearized pendulum term in the linearized state-space equations. The third set was a linearized state-space design model, which contained no pendulum term. The first two sets were simulation models used for evaluation of analytical results; the last set was used for the actual RMLA control law design. A discussion of the

techniques used to identify parameters for the plant equations from experimentally obtained data are presented in appendix A. A study of the relative moment contribution of the pendulum term with respect to the moment due to control-surface deflections was performed to justify the exclusion of the pendulum term in the design model. The details of this study are presented in appendix B, but results from the study are presented later in this section.

Nonlinear model. Equation (1) can be expressed in state-space form as

$$\dot{\mathbf{x}} = \mathbf{A}\mathbf{x} + \mathbf{B}\mathbf{u} + \mathbf{B}_e u_e \tag{2a}$$

$$u_e = \sin\phi \tag{2b}$$

where

$$\mathbf{x} = \{\, \dot{\phi} \quad \phi \,\}^T$$

$$\mathbf{u} = \{\, \delta_{\mathrm{LEO_L}} \quad \delta_{\mathrm{TEO_L}} \quad \delta_{\mathrm{TEI_L}} \quad \delta_{\mathrm{LEO_R}} \quad \delta_{\mathrm{TEO_R}} \quad \delta_{\mathrm{TEI_R}} \,\}^T$$

$$\mathbf{A} = \begin{bmatrix} \dfrac{L_p}{I_{xx}} & 0 \\ 1 & 0 \end{bmatrix}$$

$$\mathbf{B} = \begin{bmatrix} \dfrac{L_{\delta_{\mathrm{LEO_L}}}}{I_{xx}} & \dfrac{L_{\delta_{\mathrm{TEO_L}}}}{I_{xx}} & \dfrac{L_{\delta_{\mathrm{TEI_L}}}}{I_{xx}} & \dfrac{L_{\delta_{\mathrm{LEO_R}}}}{I_{xx}} & \dfrac{L_{\delta_{\mathrm{TEO_R}}}}{I_{xx}} & \dfrac{L_{\delta_{\mathrm{TEI_R}}}}{I_{xx}} \\ 0 & 0 & 0 & 0 & 0 & 0 \end{bmatrix}$$

$$\mathbf{B}_e = \begin{bmatrix} -\dfrac{mgl}{I_{xx}} \\ 0 \end{bmatrix}$$

and equation (2b) includes the nonlinear pendulum term explicitly.

An iterative, variable step Kutta-Merson method was used to solve this system analytically. This integration process is based conceptually on the discretization of the differential equations that represent the model. In this method, an initial value for u_e is assumed, and equation (2a) is then solved for $\dot{\phi}$ and ϕ for the next value of t. The value of ϕ is then used in (2b) to define the next value of u_e. The process is repeated for successive values of t over the time interval desired. Simulations were performed with this process in the MATRIX$_\mathrm{X}$/SystemBuild simulation tool developed by Integrated Systems, Inc., and described in reference 13.

Linear model. Equations (2a) and (2b) are linearized by assuming $\sin\phi \approx \phi$, which results in the following linearized model:

$$\dot{\mathbf{x}} = \mathbf{A}\mathbf{x} + \mathbf{B}\mathbf{u} - \frac{mgl}{I_{xx}}\phi \tag{3}$$

By combining the pendulum term with the term $\mathbf{A}\mathbf{x}$ of equation (2a), a linearized state-space representation may then be written as

$$\dot{\mathbf{x}} = \mathbf{A}_l\mathbf{x} + \mathbf{B}\mathbf{u} \tag{4}$$

where

$$\mathbf{A}_l = \begin{bmatrix} \frac{L_p}{I_{xx}} & -\frac{mgl}{I_{xx}} \\ 1 & 0 \end{bmatrix}$$

and $\mathbf{x}$, $\mathbf{u}$, and $\mathbf{B}$ are defined as for equations (2a) and (2b).

Effect of Pendulum Term on Plant Equations of Motion

Because the pendulum effect due to mass eccentricity is not representative of free-flying airplanes and to establish a synthesis process that is consistent with free-flying airplane equations of motion, it was desirable to remove the pendulum term from the design model equations used for control law synthesis. An analytical study was performed to quantify the pendulum effect relative to the effect of control-surface deflections during rolling maneuvers. This study was designed to determine the relative contribution of each term to the total rolling moment defined by equation (1). Simulations were performed with a preliminary set of equations to represent the AFW wind tunnel model described by equations (2a) and (2b), and the control law structure illustrated in figure 8, which allowed all control surfaces to be commanded by a single ramp-on/hold input. Details of this study are discussed in appendix B, and the results of the various terms contributing to total rolling moment are shown in figure 9. The integrals over time of the pendulum contribution, $\mathcal{M}_m$, relative to control-surface deflection contribution, $\mathcal{M}_\delta$, are shown in figure 10. The effect of the pendulum contribution is small relative to the effect of control-surface deflections for rolling maneuvers ($t_F < 1$ sec). To summarize, this study showed that the contribution to total rolling moment of the pendulum term relative to control-surface deflections was not significant during fast (less than 1 sec) rolling maneuvers of the AFW wind tunnel model.

Design-Model Equations of Motion

Based on the results of the pendulum-effect study described in the previous section, and the desire to simplify the control law synthesis procedure, the pendulum term was removed from equation (2a) to form the design-model equations of motion in state-space form

$$\dot{\mathbf{x}} = \mathbf{A}\mathbf{x} + \mathbf{B}\mathbf{u} \tag{5}$$

where $\mathbf{x}$, $\mathbf{u}$, $\mathbf{A}$, and $\mathbf{B}$ are defined in the same way as for equations (2a) and (2b). Furthermore, the wind tunnel model was rolled during tests at moderate to fast speeds ($t_F < 1$ sec) to minimize the pendulum contribution. However, the evaluation models used to generate the analytical results, which are compared with wind tunnel test results, include either the nonlinear or linearized pendulum term.

Plant Output Equations

Besides defining the roll angle and roll rate as output quantities in the equations of motion, additional outputs of interest for RMLA control law design are the torsion and bending moments, M_{t_j} and M_{b_j}. Equations (6a) and (6b) define the basic load equation for each of these loads

$$M_{t_j} = \frac{\partial M_{t_j}}{\partial \dot{\phi}}\dot{\phi} + \frac{\partial M_{t_j}}{\partial \phi}\phi + M_{0_{t_j}} + \sum_{i=1}^{6} \frac{\partial M_{t_j}}{\partial \delta_i}\delta_i \tag{6a}$$

$$M_{b_j} = \frac{\partial M_{b_j}}{\partial \dot{\phi}}\dot{\phi} + \frac{\partial M_{b_j}}{\partial \phi}\phi + M_{0_{b_j}} + \sum_{i=1}^{6} \frac{\partial M_{b_j}}{\partial \delta_i}\delta_i \tag{6b}$$

where M_{t_j} and M_{b_j} are loads computed at the locations of the torsion- or bending-moment strain gauges. Subscript j may be LI (left inboard), LO (left outboard), RI (right inboard), or RO (right outboard). The quantity δ_i is one of six control surfaces: $\delta_{\mathrm{LEO_L}}$, $\delta_{\mathrm{TEO_L}}$, $\delta_{\mathrm{TEI_L}}$, $\delta_{\mathrm{LEO_R}}$, $\delta_{\mathrm{TEO_R}}$, or $\delta_{\mathrm{TEI_R}}$. Inertial loads were not modeled.

These equations, along with roll angle and roll rate, are expressed in linearized state-space output equations describing the roll rate, roll angle, and model loads experienced during rolling maneuvers by equation (7)

$$\mathbf{y} = \mathbf{C}\mathbf{x} + \mathbf{D}\mathbf{u} + \mathbf{E} \tag{7}$$

or more explicitly,

$$\mathbf{y} = \begin{bmatrix} \{\dot{\phi} \quad \phi\}^T \\ \mathbf{y}_{\mathrm{Load}} \end{bmatrix} = \begin{bmatrix} \mathbf{I}_2 \\ \mathbf{C}_{\mathrm{Load}} \end{bmatrix} \mathbf{x} + \begin{bmatrix} \{\mathbf{0} \quad \mathbf{0}\}^T \\ \mathbf{D}_{\mathrm{Load}} \end{bmatrix} \mathbf{u} + \begin{bmatrix} \{0 \quad 0\}^T \\ \mathbf{E}_{\mathrm{Load}} \end{bmatrix}$$

where

$$\mathbf{y}_{\mathrm{Load}} = \{\, M_{t_{\mathrm{LI}}} \quad M_{t_{\mathrm{LO}}} \quad M_{t_{\mathrm{RI}}} \quad M_{t_{\mathrm{RO}}} \quad M_{b_{\mathrm{LI}}} \quad M_{b_{\mathrm{LO}}} \quad M_{b_{\mathrm{RI}}} \quad M_{b_{\mathrm{RO}}} \,\}^T$$

$$\mathbf{I}_2 = \begin{bmatrix} 1 & 0 \\ 0 & 1 \end{bmatrix}$$

$$\mathbf{C}_{\mathrm{Load}} = \begin{bmatrix} \dfrac{\partial M_\ell}{\partial \dot{\phi}} \\ \dfrac{\partial M_\ell}{\partial \phi} \end{bmatrix}$$

$$\ell = t_{\mathrm{LI}},\, t_{\mathrm{LO}},\, t_{\mathrm{RI}},\, t_{\mathrm{RO}},\, b_{\mathrm{LI}},\, b_{\mathrm{LO}},\, b_{\mathrm{RI}},\, b_{\mathrm{RO}}$$

$$\mathbf{0} = [\,0 \quad 0 \quad 0 \quad 0 \quad 0 \quad 0\,]$$

$$\mathbf{D}_{\mathrm{Load}} = \left[\frac{\partial M_{t_{\mathrm{LI}}}}{\partial \delta_i} \quad \frac{\partial M_{t_{\mathrm{LO}}}}{\partial \delta_i} \quad \frac{\partial M_{t_{\mathrm{RI}}}}{\partial \delta_i} \quad \frac{\partial M_{t_{\mathrm{RO}}}}{\partial \delta_i} \quad \frac{\partial M_{b_{\mathrm{LI}}}}{\partial \delta_i} \quad \frac{\partial M_{b_{\mathrm{LO}}}}{\partial \delta_i} \quad \frac{\partial M_{b_{\mathrm{RI}}}}{\partial \delta_i} \quad \frac{\partial M_{b_{\mathrm{RO}}}}{\partial \delta_i} \right]^T$$

$$i = \mathrm{LEO_L},\, \mathrm{TEO_L},\, \mathrm{TEI_L},\, \mathrm{LEO_R},\, \mathrm{TEO_R},\, \mathrm{TEI_R}$$

$$\mathbf{E}_{\mathrm{Load}} = \{\, M_{0_{t_{\mathrm{LI}}}} \quad M_{0_{t_{\mathrm{LO}}}} \quad M_{0_{t_{\mathrm{RI}}}} \quad M_{0_{t_{\mathrm{RO}}}} \quad M_{0_{b_{\mathrm{LI}}}} \quad M_{0_{b_{\mathrm{LO}}}} \quad M_{0_{b_{\mathrm{RI}}}} \quad M_{0_{b_{\mathrm{RO}}}} \,\}^T$$

The terms in $\mathbf{E}_{\mathrm{Load}}$ are either a steady-state torsion moment or bending moment at one of the inboard or outboard locations of the left or right wing.

Equation (7) defines the plant output equations for both the evaluation and design models. The experimentally derived parameters for these equations are shown in equations (A6) and (A7).

RMLA Control Law Synthesis

In this study the RMLA control laws were developed by observations of how incremental loads varied during simulated rolling maneuvers and how control-surface deflections affected these loads. The linear design model described by equation (5) was the basis of the RMLA design. Additionally, output equations described by equation (7) formed the basis of the load calculations. However, for the design model, the steady-state loads, M_{0_j}, were assumed to be 0 ($\mathbf{E} = 0$), which means the incremental loads were assumed to equal the output loads. For other elements in the design model, the experimentally derived parameters defined in appendix A were used.

The basic design objective for RMLA control laws was to reduce incremental loads generated during a rolling maneuver with no roll performance penalty. As mentioned in the section entitled

"RMLA Design Concept," this meant developing active RMLA control laws that would attempt to alleviate both bending- and torsion-moment wing loads during fast rolling maneuvers. Some preliminary studies that used results of control-surface roll and load effectiveness from earlier 1989 wind tunnel tests showed the trailing-edge inboard pair of control surfaces generated the largest rolling moments. However, the outboard control surfaces demonstrated a more substantial ability to affect incremental loads during rolling maneuvers. These studies implied that the outboard surfaces could be deflected a limited amount during a maneuver to alleviate loads, and any roll performance lost because of this actuation of outboard control surfaces could be regained by increased deflections of the trailing-edge inboard control surfaces. From initial simulation studies, it was found that bending- and torsion-moment loads were coupled to each other and to the angular deflections of the control surfaces. Results of the control surface load effectiveness evaluations, described later in this section, verify these initial studies. This coupling of the loads indicated that simplifying the control objective by targeting the reduction of a single type of load was plausible. Results of another simulation study, summarized in figure 11, showed that when the inboard control surfaces were used, torsion-moment peak incremental loads were significantly larger relative to their steady-state values than the respective bending-moment loads. Based on these preliminary results, the original RMLA objective was modified to target reductions of only the peak incremental torsion moments rather than those of both the torsion and bending moments. This modification still met the intent of the original research objective. However, by designing control laws to reduce only these key loads, makes the design effort significantly simpler, although care must be taken that the trade-offs (in this case, increases in the peak incremental bending moments) are not too severe.

Thus, the RMLA control laws were formulated to use the trailing-edge inboard control surface pair for maintaining roll performance of the vehicle while outboard control surfaces (leading or trailing edge) were used to reduce peak incremental torsion-moment loads.

Synthesis Procedure

The RMLA control law synthesis procedure used herein involves four steps, which are outlined below.

1. Evaluate control-surface load effectiveness

   Evaluate the ability of each control surface to affect change in roll and loads during fast rolling maneuvers.

2. Determine potential control law form

   Establish effective control-surface combinations and a feedback control law form that can potentially reduce dynamic loads.

3. Determine control law gains

   Iterate control system gains for the various control-surface combinations to determine a set of gains that effectively reduces dynamic loads during specified rolling maneuvers.

4. Determine control system stability and robustness

   Check whether the stability margins are adequate after iterating for a set of control system gains.

Synthesis Steps

The following section describes the development of the particular RMLA control laws which are described herein.

Evaluate control surface load effectiveness. A qualitative procedure was established to evaluate the ability of each outboard control surface to change incremental loads generated during a rolling maneuver; in other words, the load effectiveness of each outboard control was evaluated. This method provided sufficient information to determine which direction the leading-edge outboard and trailing-edge outboard control-surface pairs should be deflected during rolling maneuvers to produce decreases in the incremental loads. For this evaluation, the experimentally determined plant equations defined in appendix A for dynamic pressure $q = 150$ psf was used.

Simulations were performed with the same control law structure as the mass eccentricity study, which allowed all surfaces to be commanded by a single external ramp-hold input (fig. 8). Right and left control surfaces were deflected differentially with a positive deflection of a control-surface pair being defined as the left control surface deflected upward (negative) and the right downward (positive).

The systematic procedure used to define operation of the outboard control was straightforward. The procedure was simply to apply specified positive and negative outboard control-surface (differential) deflections during simulated rolling maneuvers while the trailing-edge inboard control surfaces were used to maintain a constant performance.

Five sets of incremental-load time histories were obtained. Figure 12 shows the time histories of the incremental outboard bending moment obtained for each of these simulations. The first set corresponds to a rolling maneuver performed with the trailing-edge inboard control surfaces only (baseline) to achieve a rolling performance of 90° to 0° in 0.75 sec. The maneuver was performed to determine baseline incremental outboard bending moment. The second set of incremental-load time histories corresponds to a maneuver performed with a 2° differential deflection of the leading-edge outboard control-surface pair (+LEO) while the trailing-edge inboard control-surface pair was deflected a sufficient amount to maintain the roll performance of 90° to 0° in 0.75 sec. The third set of incremental-load time histories was obtained in a similar manner except that the leading-edge outboard control surface was deflected −2° (−LEO) during the maneuver. The fourth and fifth sets of incremental-load time histories were obtained by performing the same rolling maneuvers with the leading-edge outboard control-surface deflections held at 0° and the trailing-edge outboard control-surface deflections specified to be 2° and −2° during two separate rolling maneuvers, (+TEO and −TEO, respectively). The dashed line indicates the time at which the simulated rolling maneuvers passed 0°.

By plotting the five sets of incremental loads, it can be seen how outboard control-surface deflections affect the incremental outboard bending moment. As can be seen in figure 12, negative deflections of both outboard control-surface pairs were found to cause decreases in outboard incremental bending loads. Similar results were obtained for the inboard incremental bending loads and inboard incremental torsion loads; however, decreases in outboard incremental torsion loads resulted only from negative deflections of the outboard trailing-edge control surfaces. A summary of the qualitative results of this study is shown in table 1. Increase or decrease indicates whether the peak incremental loads increased or decreased when compared with the peak incremental loads of the baseline maneuver. Control-surface differential deflection is also indicated. Based on these results, the most effective control surfaces for reducing all incremental loads would most likely be the outboard trailing-edge control-surface pair.

Determine potential control law form. Since the rolling maneuvers were defined in terms of time to roll, it was determined that the command to roll would be proportional to roll rate. It was also observed during the simulations that the incremental loads tended to be (linearly) proportional to the roll rate. Thus, direct feedback of the roll rate to control surfaces could reasonably be used to counteract the incremental loads, as well as to roll the model. The trailing-edge inboard control surfaces were chosen to maintain roll performance while the

outboard control surfaces were used to reduce incremental loads. In summary, the RMLA control laws described herein were designed to (1) actuate the trailing-edge inboard control surfaces in the positive direction differentially (left upward, right downward) to effect roll, (2) actuate the leading-edge outboard and/or trailing-edge outboard control-surface pairs in the negative direction differentially (left downward, right upward) to reduce loads, and (3) adjust all the control-surface deflections based on the roll rate.

Based on the above reasons, the RMLA control law structure illustrated in figure 13 was selected as the basic RMLA control law form to be used. The structure includes roll-rate feedback to the trailing-edge inboard, leading-edge outboard, and trailing-edge outboard control-surface pairs. Left and right wing control surfaces in each pair are deflected differentially. In addition to the roll-rate feedback, the roll-rate command describing the desired roll-rate performance is also sent to the trailing-edge inboard control-surface pair. Outboard control surfaces are commanded only by roll-rate feedback.

Since the first flexible mode frequency was above 7 Hz, a 8.75-Hz low-pass filter defined by

$$T_{\delta_i} = \frac{4.65(10^5)}{s^3 + 206.71s^2 + 14804s + 4.65(10^5)} \tag{8}$$

was included in each loop of the system to minimize the effect of the RMLA control laws on the flexible modes that would be present during tests and to smooth the input command.

The RMLA control laws can be expressed in linearized state-space form as

$$\left.\begin{aligned} \dot{\mathbf{x}}_c &= \mathbf{F}_c\mathbf{x}_c + \mathbf{G}_f\mathbf{z}_f + \mathbf{G}_{\text{com}}\dot{\phi}_{\text{com}} \\ \mathbf{u} &= [\mathbf{D}_c\mathbf{H}_c]\mathbf{x}_c + \mathbf{E}_f\mathbf{z}_f + \mathbf{E}_{\text{com}}\dot{\phi}_{\text{com}} \end{aligned}\right\} \tag{9}$$

where

$$\mathbf{E}_{\text{com}} = [\,K_{\text{com}} \quad 0 \quad 0 \quad 0\,]^T$$

$$\mathbf{E}_f = [\,0 \quad K_{\text{TEI}} \quad K_{\text{TEO}} \quad K_{\text{LEO}}\,]^T$$

and $\mathbf{x}_c$ represents the controller states, $\mathbf{z}_f$ the feedback control input $\dot{\phi}$, and $\dot{\phi}_{\text{com}}$ the commanded roll rate.

Determine control law gains. Initial gains were chosen from the information determined during the control-surface effectiveness study and the RMLA control law structure defined in figure 13. The most important aspect of the RMLA control law design was that the control laws produce outboard control-surface deflections during a rolling maneuver to counteract incremental loads. In addition, it was necessary that the control laws produce reasonable control-surface deflections and rates that did not saturate the actuators at dynamic pressure ranges of 150 to 250 psf. A target rolling maneuver performance criterion of 90° to 0° in 0.75 sec was selected for the RMLA design. The input gain K_{com} and feedback gains K_{TEI}, K_{TEO}, and K_{LEO} were then iterated until the model met its target performance while reducing analytically predicted peak incremental loads and meeting robustness design objectives analytically.

Three control laws, referred to herein as A, B, and baseline, were developed with experimentally derived equations of motion and equations of plant output. Each control law was designed to meet test objectives at a design q = 150 psf and a corresponding Mach number of 0.33. The control laws were then also evaluated for the design model at q = 250 psf and

Mach number of 0.44. Control law A was defined by roll-rate feedback to the trailing-edge inboard control-surface pair and from the trailing-edge outboard control-surface pair ($K_{\mathrm{LEO}} = 0$). Control law B was defined by roll-rate feedback to the trailing-edge inboard control-surface pair and to the leading-edge outboard control-surface pair ($K_{\mathrm{TEO}} = 0$). Finally, the baseline control law was defined by roll-rate feedback from the trailing-edge inboard control-surface pair only ($K_{\mathrm{TEO}} = 0$ and $K_{\mathrm{LEO}} = 0$). A summary of control system gains is listed in table 2.

Determine control system stability and robustness. System stability was determined analytically for each closed-loop system at the two design conditions, $q = 150$ and 250 psf, with each of the three control laws defined previously. The system stability was determined by performing an eigenvalue analysis on the linearized state-space model of the closed-loop system for each control law. For these analyses, the plant was defined by equations (10), where $\dot{\phi}$ is the only output used for the RMLA feedback control law

$$\left.\begin{aligned} \dot{\mathbf{x}} &= \mathbf{A}\mathbf{x} + \mathbf{B}\mathbf{u} \\ \mathbf{z}_f &= \mathbf{C}_f\mathbf{x} \end{aligned}\right\} \tag{10}$$

where $\mathbf{x}$, $\mathbf{u}$, $\mathbf{A}$, and $\mathbf{B}$ are defined by equation (5) and

$$\mathbf{z}_f = \dot{\phi}$$

$$\mathbf{C}_f = [\,1 \quad 0\,]$$

For the stability analyses discussed herein, the experimentally defined models described in appendix A were used for the equations, and the roll-rate command $\dot{\phi}_{\mathrm{com}}$ was assumed to be 0.

Each of the three control laws presented were stable. Table 3 shows the eigenvalues of the closed-loop system for each of the RMLA control laws at $q = 150$ psf that correspond to the model parameters defined in equation (A6) and those values for $q = 250$ psf that correspond to model parameters defined in equation (A7). Note that all eigenvalues have negative real parts with zero imaginary parts and therefore lie in the left complex plane, which implies a stable closed-loop system. The eigenvalues for the baseline system are not shown.

Once system stability is established, stability margins can be determined with the method described in reference 14. The stability margins for each of the designed RMLA control laws was predicted in terms of simultaneous gain and phase changes in each of the loops of a multiloop system. The universal gain and phase margin diagram shown in figure 14, which is based on figure 2 in reference 14, provides a mechanism for predicting regions of guaranteed stability in an operating frequency range. Reference 14 shows that the stability of the perturbed system is guaranteed provided the minimum singular value of the linear system return difference matrix is greater than $\overline{\sigma} = \mathbf{L}^{-1} - \mathbf{I}$.

To determine the stability margins in a multiloop system, the system return-difference matrix at the plant input must be determined and the minimum singular values calculated. This matrix is defined by $[\mathbf{I} + \mathbf{G}\mathbf{H}(i\omega)]$, where

$$\mathbf{G} = -[\mathbf{D}_c\mathbf{H}_c(\mathbf{I}s - \mathbf{F}_c)^{-1}\mathbf{G}_f + \mathbf{E}_f] \tag{11}$$

is the controller transfer matrix and

$$\mathbf{H} = [\mathbf{C}_f(\mathbf{I}s - \mathbf{A})^{-1}\mathbf{B}] \tag{12}$$

is the plant transfer matrix. The closer the minimum singular value is to 0 at any frequency, the less robust the system is to modeling errors. The stability margins were determined for

the $q = 150$ psf design model. For this model, the closed-loop system with the baseline control law implemented was determined analytically to have a minimum singular value of 0.49. The closed-loop systems, with control laws A and B implemented, were determined to have singular values of 0.79 and 0.77, respectively. In figure 14, a horizontal line drawn at $\sigma_{\min} = 0.79$ and intersecting the 20° phase line at −4.2 dB and 12.8 dB indicates that control law A has a guaranteed minimum gain margin of −4.2 dB and 12.8 dB with at least a 20° phase perturbation margin in all loops. This process illustrates the use of the diagram to determine gain and phase margins for control law A. The RMLA control law B and the baseline control law have guaranteed minimum gain margins of −4 dB and 11 dB and −2 dB and 5 dB, respectively, with 20° phase perturbation margin in all loops. For other phase margin perturbations, different gain margins could be achieved.

Wind Tunnel, Test Procedures, and Data Reduction for RMLA Performance Evaluation

Wind Tunnel

The Langley Transonic Dynamics Tunnel (TDT) is a closed-circuit, continuous flow wind tunnel with a 16-ft-square test section with cropped corners. It operates at stagnation pressures from near vacuum to slightly above atmospheric pressure and at Mach numbers to 1.2. Tunnel Mach number may be varied simultaneously or independently with dynamic pressure. Either air or a heavy gas can be used as the test medium. During the current investigation, air was used as the test medium. The TDT is equipped with hydraulic bypass valves, which may be opened rapidly to reduce test section dynamic pressure and Mach number when flutter is encountered. A more detailed description of the TDT is presented in reference 15.

Test Procedures

Initially, control laws A and B and the baseline control law were tested at tunnel test conditions of $q = 150$, 200, and 250 psf and Mach numbers of 0.33, 0.39, and 0.44, respectively. The model was configured for each of these tests so that open-loop flutter would not be incurred. Each rolling maneuver controlled by RMLA commenced with the model positioned at a roll angle of 90° and was terminated shortly after the model rolled through 0°. Maneuvers at $q = 150$ and 200 psf were performed with the tip ballast coupled; however, those at $q = 250$ psf were performed with the tip ballast decoupled to raise the open-loop flutter dynamic pressure above the test dynamic pressure. Figure 15 shows the operating envelope in air for the TDT. The test points at which single-function RMLA control laws (no flutter suppression control law active) were tested with the tip ballasts coupled are indicated by solid circles, and the test point with the tip ballasts decoupled is indicated by a solid square. The open-loop flutter point is also identified. Table 4 summarizes the conditions for single-function RMLA control law tests.

Rolling maneuvers were also performed above the open-loop flutter dynamic pressure at $q = 250$ and 260 psf with the tip ballast coupled. These test points are identified with open circles in figure 15. For these maneuvers, RMLA control law B was implemented simultaneously with an active flutter suppression system (FSS) by using the control law described in reference 16. During these multiple-function maneuvers, the rolling maneuvers commenced with the model positioned at 70° roll angle instead of 90° and were terminated as the model rolled through −20° because at 90° the measured dynamic loads were too close to the preselected load limits of the trip system for the wind tunnel model. This adjustment of the rolling maneuver starting point and termination point allowed less interruptions of the test because the multifunction rolling-maneuver tests could be conducted in a dynamic load range where the trip system was less likely to trigger the tunnel bypass system. Table 5 summarizes conditions for this multiple-function RMLA + FSS test.

Figure 16 is a description of how the RMLA controllers were commanded during tests and how the roll-rate commands were implemented on the digital controller. The model was first rolled to and held at its initial roll position with the RTS. When ready for a rolling maneuver, control of the model was switched to the RMLA control system within the digital controller, and control of the model by the RTS was discontinued. At this point, control-surface commands were determined by a specified RMLA control law (control law A or B, or the baseline control law). As shown in figure 16, the roll rate was commanded by a ramp-on/hold input during the maneuver. Different roll rates could be specified to achieve desired time-to-roll performance requirements. A ramp-off roll-rate command was used to terminate the maneuver after the model passed through the termination roll angle. When the model roll rate was below 5 deg/sec (denoted $\dot{\phi}_{\text{cap}}$ in the figure), digital control of the model was switched from RMLA back to RTS once again. To simplify the control law design process, the rolling-maneuver load control laws were only designed to reduce loads for the portion of the maneuver prior to the point where the roll-rate commands were ramped off. This point is referred to as the time to roll, identified as t_F in figure 16. The comparison of the results described herein are for the design region from 0 to t_F.

For both the single-function RMLA tests and the multiple-function tests, rolling maneuvers were repeated at each test point for several different roll-rate commands defined by a scale factor times a nominal command input to assure that data obtained were in the performance range of interest. These scale factors ranged from 0.8 to 1.4 and are listed in figure 17.

Data Reduction for RMLA Performance Evaluation

Before describing the results obtained from wind tunnel tests, a brief discussion of the data reduction method used to evaluate the RMLA performance is necessary. First, peak incremental loads had to be extracted from test data for each rolling maneuver performed. Four incremental loads were examined: outboard incremental bending moment $\Delta M_{b_{\text{O}}}$, inboard incremental bending moment $\Delta M_{b_{\text{I}}}$, outboard incremental torsion moment $\Delta M_{t_{\text{O}}}$, and inboard incremental torsion moment $\Delta M_{t_{\text{I}}}$. These incremental loads were defined to be one-half the right wing incremental load (with respect to the initial steady-state load value) minus one-half the corresponding left wing incremental load, respectively for each load as described by

$$\left.\begin{aligned} \Delta M_{b_j}(t) &= \frac{1}{2}\left\{\left[M_{b_{\text{R}j}}(t) - M_{ss_{b_{\text{R}j}}}\right] - \left[M_{b_{\text{L}j}}(t) - M_{ss_{b_{\text{L}j}}}\right]\right\} \\ \Delta M_{t_j}(t) &= \frac{1}{2}\left\{\left[M_{t_{\text{R}j}}(t) - M_{ss_{t_{\text{R}j}}}\right] - \left[M_{t_{\text{L}j}}(t) - M_{ss_{t_{\text{L}j}}}\right]\right\} \end{aligned}\right\} \tag{13}$$

where j = O or I and the terms with ss as a subscript represent the corresponding steady-state values. The steady-state loads at the start of each rolling maneuver are summarized in table 6 for each dynamic pressure. Table 7 shows corresponding static load limits for each type of load to provide a reference level for each load.

Peak incremental loads equal to the maximum absolute value of the incremental loads that occurred during each rolling maneuver were computed by

$$\left.\begin{aligned} \overline{\Delta M_{b_j}} &= \max_t \left|\Delta M_{b_j}(t)\right| \\ \overline{\Delta M_{t_j}} &= \max_t \left|\Delta M_{t_j}(t)\right| \end{aligned}\right\} \tag{14}$$

where j = O or I.

Results and Discussion

In this section, incremental-load time histories obtained during RMLA-controlled rolling maneuvers are compared to baseline loads, and the reduction in peak incremental loads are presented. The resulting load alleviation achieved with RMLA control law A and control law B are presented and the performance of the two control laws are also compared. Finally, an evaluation of the multiple-function performance of RMLA control law B implemented with a flutter suppression control law is presented.

Experimental Results

Results were calculated with equations (13) and (14) for all RMLA-controlled rolling maneuvers and the baseline rolling maneuvers. The resulting incremental loads and peak incremental loads for all maneuvers and test conditions are too numerous to discuss and compare in this paper; however, typical results are shown and comparisons are made in the subsection entitled "Time History Comparisons of Incremental Loads." Discussion of incremental-load reductions and summaries of results are presented in subsections entitled "Typical Load Alleviation Results" and "Overall Analysis of Experimental Results," respectively.

Time history comparisons of incremental loads. Some typical time history results obtained during wind tunnel evaluation for RMLA control laws A and B are shown in figures 18 and 19, respectively. In both of these figures, the incremental loads obtained during a rolling maneuver controlled by the specified RMLA control law and a corresponding baseline maneuver having nearly the same performance time to roll 90° are compared. Since the performance times are nearly the same, a comparison can be made between the actual RMLA and the baseline load time histories, rather than comparing only the RMLA-controlled peak incremental loads with interpolated peak values from baseline rolling maneuvers. The rolling maneuver was a 90° to 0° roll at $q = 200$ psf with a performance time t_F of 0.66 sec for control law A, 0.645 sec for control law B, and 0.65 sec for the baseline control law. Roll-rate and roll-angle time histories are shown in parts (a) and (b), respectively, of figures 18 and 19. The vertical dashed line indicates the approximate point in time at which the RMLA-controlled rolling maneuver was considered terminated, and the roll-rate command ramped off. Since the following discussion can generally be applied to the results shown for both controllers, only results of control law B corresponding to figure 19 will be discussed in further detail, but the results of control law A (fig. 18) are presented for completeness.

Decreases in incremental torsion moments are shown in figures 19(c) and 19(d) for most of the rolling maneuver from 90° to 0°. There is a substantial decrease in peak incremental torsion moments. The outboard and inboard torsion moments of 495.1 and 1565 in-lb, respectively, at 0.49 sec for the baseline control law decrease to 265.6 and 885.8 in-lb, respectively, at 0.4 sec for control law B. This substantial reduction in peak incremental torsion moments is typical of all the RMLA-controlled rolling maneuvers.

Similar comparisons for the incremental bending moments, figures 19(e) and 19(f), indicate increases in the peak incremental load for the outboard and inboard bending moments, but all the peak incremental loads are more nearly the same for the RMLA-controlled maneuver. One incremental load that is approximately three times larger than all the others for the baseline maneuver, namely the inboard torsion moment, is brought within the same level of load as all the others. Since the design criteria did not include the peak incremental bending moments, it is not surprising to see an increase in these as a result of lowering the peak incremental torsion moments.

Figure 18 shows similar decreases and increases in incremental loads for control law A; however, the significance of the load increases to the severity of trade-off between decreases

and increases in incremental loads is still to be determined. The next two sections address this issue in more detail.

Typical load alleviation results. Table 8 summarizes the percent changes in peak incremental loads shown in figures 18 and 19 for both control laws A and B, and bar graphs of these changes are shown in figure 20. Figure 20(a) summarizes the changes for control law A in peak incremental loads relative to the baseline. The figure shows that the peak outboard incremental torsion moment is reduced by 27.4 percent relative to the baseline case and peak inboard incremental torsion moment is reduced by 52.3 percent. There is a 14.7 percent increase in the peak value of inboard incremental bending moment. Peak outboard incremental bending moment for control law A, however, is shown to increase by approximately 2.5 times with respect to the baseline.

Figure 20(b) illustrates similar results from the tests of RMLA control law B. As before, reductions in incremental torsion moments were achieved. Peak outboard incremental torsion moment was reduced by 46.4 percent and peak inboard incremental torsion moment was reduced by 43.4 percent. Increases, however, are seen in both outboard and inboard incremental bending-moment peak values of 39.7 percent and 16.0 percent, respectively.

To gauge the significance of these results for each load, a comparison can be made between changes in peak incremental loads and the static load limits, which are listed in table 7. For instance, the increase over the baseline of 16.0 percent in peak inboard incremental bending moment shown in figure 20(b) is less than 0.3 percent of the minimum inboard bending-moment static load limit. Similarly, the percentage increase in peak outboard incremental bending moment represents less than 2.1 percent of the minimum outboard bending-moment static load limit. On the contrary, the percentage decreases in peak outboard and inboard incremental torsion moments represent larger percentages (16.1 percent and 7.6 percent) of their respective minimum torsion-moment load limits.

Table 9 summarizes the percent changes in incremental loads relative to minimum static load limits for both control laws. In both of these cases, the changes in the outboard torsion moment are significant since the amount of load alleviation because of implementation of the RMLA control law represents a substantial portion of the capacity of each wing to support outboard torsion moments. The small percentage increases in the bending moments because of control law B are considered to be an inconsequential trade-off for the significant percentage decreases in torsion moments relative to the minimum static load limits. Note that the 12.8 percent increase in peak incremental outboard bending moment relative to the minimum static load limits for control law A might indicate a significant trade-off penalty for the decreases in torsion-moment peak incremental loads, warranting further investigation.

Overall analysis of experimental results. This section provides an analysis of the results of all the rolling maneuvers performed in the TDT with the two RMLA control laws described herein and the baseline control law. The same trends indicated in the previous comparisons occurred between all the RMLA-controlled maneuvers and the baseline maneuvers. The peak incremental loads were calculated from the experimental data with equations (14) for all the rolling maneuvers performed and these results are presented in table 10. The RMLA-controlled rolling maneuvers had different performance times from the baseline maneuvers. Test time did not permit performing additional maneuvers to obtain the same performance times. Because it was necessary to compare the RMLA maneuvers with baseline maneuvers with the same performance times, peak incremental loads obtained for baseline maneuvers were interpolated as a function of performance time to correspond to performance times equal to those achieved during RMLA-controlled maneuvers. These calculations are presented in table 11, and the interpolated values were used for all the results discussed subsequently.

The results in table 11 show that the peak incremental torsion moments are decreased in every case for both control laws. This is consistent with the control law design criteria. Since the results for bending moments are mixed, and in some cases might represent too great a trade-off penalty, it is necessary to evaluate these results with other criteria. The relative importance of the peak incremental change in load can be compared with either the average of the initial steady-state loads at a 90° roll angle and a 0 deg/sec roll rate of both wings or the minimum static load.

Figure 21 shows graphically the percent changes in the peak incremental loads between all RMLA-controlled maneuvers and the baseline maneuvers with respect to the average steady-state loads for the three dynamic pressures: $q = 150$, 200, and 250 psf. The percent changes are plotted with respect to t_F. Each percentage shown in figure 21 is in terms of its respective initial steady-state load value so that relative importance of the change with respect to the initial load can easily be assessed. Increasing time implies slower rolls and less incremental change. For control law A and control law B, the rolling maneuvers produced both positive and negative percentage changes. A negative percentage indicates a decrease in the incremental load from the peak baseline incremental loads for either control law.

For control laws A and B, load reductions for all cases of the inboard and outboard torsion moment ranged from about 21 percent at $q = 150$ psf for control law A to as much as 140 percent at $q = 250$ psf for control law B (fig. 21). In general, the reductions tend to increase with increased dynamic pressure. In most cases, for all three dynamic pressures of $q = 150$, 200, and 250 psf, rolling the model slower resulted in decreased reductions in the peak incremental torsion moments. It can be seen from figure 21 that the reductions for outboard torsion moment are greater for control law B, which used the outboard leading-edge control surfaces for load reduction, and those for inboard torsion moment were greater for control law A, which used the outboard trailing-edge control surfaces for load reduction. Furthermore, the combined reductions in peak incremental torsion moments outweigh the combined increase in peak incremental bending moments in all cases for both control laws.

Still to be resolved is whether the increase in peak incremental outboard bending moment represents too severe a trade-off penalty. Thus, percent changes relative to corresponding minimum static load limits were calculated. These results are compared in table 12 with the percent changes relative to the peak incremental baseline load and the initial steady-state loads. The results tend to indicate that in the case of control law A, in which peak incremental bending moments decidedly increase, the increase is not significantly large with respect to the load limits. To verify this further, a comparison of the peak incremental baseline load, peak incremental RMLA-controlled load and the initial steady-state load relative to the static load limits was performed. Table 13 summarizes these results. The results for control law A at $q = 200$ psf are shown in figure 22. Those for control law B are shown in figure 23. These figures depict the relative percent difference between the RMLA-controlled loads and the baseline in terms of the load limit percentages for all the loads. The percentage of steady-state load relative to the static load limit is shown as a dark vertical bar. The percentage change in peak incremental load relative to the static load limit is added to each of these bars. In each case, the RMLA-controlled load is plotted to the right of the baseline load. As can be seen from these figures, the only increase in incremental load because of RMLA control of significant interest is that for outboard bending moment for control law A shown in figure 22(c). It can be seen that the total load change is less than 50 percent of the static load limit. In fact, the total load is less than 50 percent for all RMLA-controlled loads for this dynamic pressure. Furthermore, very little change in inboard bending moment occurs from use of either leading- or trailing-outboard edge control surfaces.

Summary of experimental results. In general, control law B, which used the leading-edge outboard control-surface pair, resulted in greater reductions in outboard incremental torsion moments than control law A. The reverse is true for the inboard incremental torsion moments. This suggests that, for the AFW wind tunnel model, the leading-edge outboard control-surface pair is more effective at reducing the outboard incremental torsion moments than the trailing-edge outboard control-surface pair. Likewise, the trailing-edge outboard control-surface pair is more effective in decreasing inboard incremental torsion moments. In both cases, the targeted design goal, namely, reducing peak incremental torsion moments, was substantially met.

Control law A and control law B differed more significantly in how peak incremental bending moments were affected during rolling maneuvers. It can be observed from table 12 that peak values of incremental bending moments increased 285 percent relative to a baseline maneuver for maneuvers controlled by control law A and less than 42 percent increases for comparable maneuvers controlled by control law B; however, these increases proved to be only 56.6 percent increase with respect to the initial loads, and only 17.6 percent with respect to the minimum static load limit. Furthermore, it was demonstrated that in all cases, the RMLA-controlled load plus the corresponding initial steady-state load does not exceed 57 percent of the static load limit.

In general, control law B demonstrated the better overall RMLA characteristics relative to the limit loads. (Compare fig. 23 with fig. 22.) The percent changes for bending-moment loads with respect to the steady-state loads were shown to be small. These results confirm initial perceptions that only torsion moment need to be targeted for load reduction in designing an RMLA control law, as stated in the RMLA Design Concept section. With control law B, substantially large reductions were achieved in both inboard and outboard incremental torsion moments without significant increases in incremental bending moments. A significantly higher reduction was achieved in outboard torsion moment with control law B than for either the inboard or outboard torsion moments for control law A. Since the reductions relative to static load limits are most significant for outboard torsion moments, control law B is considered to be the more effective of the two for rolling-maneuver load alleviation.

Comparison of Experimental and Analytical Results

To evaluate how well the analytical models could be used to predict load reduction during controlled rolling maneuvers, simulated maneuvers were performed on the computer at dynamic pressures of $q = 150$ and 250 psf and at performance times of 0.65 and 0.75 sec with the nonlinear equations of motion (2a) and (2b) and the output equation (7). Experimentally derived parameters defined by equations (A6) and (A7) were used in the equations. Figure 24 shows the percent changes between simulated and experimental peak incremental torsion moments obtained during RMLA-controlled maneuvers relative to those obtained during baseline-controlled maneuvers with the same performance times. Dashed lines indicate analytical results and the solid lines show the experimental results. Figures 24(a) and 24(c) show results for control law A, and 24(b) and 24(d) for control law B.

As can be seen from figure 24, the analytical model, in general, predicts the trends in reduction for the incremental torsion moments; however, the analytical model is conservative in predicting the absolute value of reduction in all cases.

Multiple-Function Control Law Performance Results

Successful rolling maneuvers 6 percent and 11 percent above the open-loop flutter dynamic pressure were achieved in tests with RMLA control law B and a flutter suppression control law implemented simultaneously on the digital controller (ref. 16). Flutter did not occur during the maneuvers, which implies that the flutter suppression control law was suppressing the instability

during roll. It was not possible to quantify incremental load reduction since time did not allow baseline data at the same dynamic pressures with the AFW model in the tip-ballast-coupled configuration to be obtained. Thus, a qualitative evaluation of load reduction could not be made above open-loop flutter. However, based on comparisons of incremental loads with the FSS control law operating at subcritical dynamic pressures for which comparable baseline data were available, namely $q = 150$ and 200 psf, it is likely that incremental load reduction occurred. Since rolling maneuvers had to be ramped off quickly to avoid exceeding the roll angle of the model on the sting, load trip limits were incurred during the ramp-off portion of the rolling maneuvers in some cases. However, trip limits based upon static load limits were incurred only when the roll command was ramped off. Since the RMLA control laws were not designed to reduce loads during the ramp-off portion of the roll command, and trip limits were not incurred during the ramp-on/hold portion of the rolling maneuvers, it can be stated that control law B did not induce excessive incremental loads during rolling maneuvers above the open-loop flutter dynamic pressure.

By observing control surface deflection time histories during a rolling maneuver, it was seen that the RMLA and flutter suppression control laws operated simultaneously without significant interference. Figure 25 shows control surface deflections during a roll which occurred in 0.63 sec at $q = 250$ psf with simultaneous operation of RMLA and FSS. The time histories are for right wing control surfaces only. The dashed lines indicate the point in time at which the roll was terminated. The leading-edge outboard and the trailing-edge inboard control-surface deflections due to RMLA are shown in figures 25(a) and 25(b). Trailing-edge outboard control-surface deflection is due to the flutter suppression control law and is shown in figure 25(c). Figure 25(c) shows that the trailing-edge outboard control surface was oscillating at about 9.5 Hz. This frequency of oscillation was due to the FSS control law for flutter suppression, during and after the rolling maneuvers.

Thus, it was demonstrated that the RMLA and flutter suppression control laws can be implemented simultaneously on the AFW digital controller and operate effectively together during rolling maneuvers at dynamic pressures 11 percent above the critical flutter dynamic pressure.

Concluding Remarks

This report provides a systematic synthesis methodology to design RMLA feedback control laws. Two relatively simple RMLA control laws, referred to herein as A and B, were designed and implemented on a digital control computer. Control law A used trailing-edge surfaces and control law B used leading-edge surfaces to alleviate loads. These control laws were experimentally evaluated and shown to effectively and reliably reduce incremental torsion loads on the AFW wind tunnel model in the Transonic Dynamics Tunnel (TDT). In addition, it was demonstrated through wind tunnel tests that a digital control computer can be used with great versatility to perform a multifunction task such as suppressing flutter and reducing loads during rolling maneuvers. The analytical model provided conservative estimates of peak incremental load reduction.

Load alleviation during controlled rolling maneuvers of a model in the wind tunnel was demonstrated. Leading-edge and trailing-edge control surfaces were actively employed by digital control to accomplish this objective.

Torsion moment reduction was targeted as the design objective, and experimental evaluation of two RMLA controllers showed up to a 61.6 percent reduction in peak incremental torsion moments when compared with those generated by corresponding baseline rolling maneuvers at equivalent dynamic pressures with the same time-to-roll performance. Incremental bending moments were evaluated. Results varied, but in general showed relatively small load changes

when compared with static load limits during the same rolling maneuver. The maximum increase was a peak incremental outboard bending moment of 17.6 percent relative to the static load limit for control law A; however, the resulting combined steady-state and peak incremental load of less than 60 percent of the static load limit was within load limit margins.

Control law B showed at least 14 percent greater reduction capability of the outboard torsion moment and at least a 31 percent reduction in inboard incremental torsion moment relative to a baseline rolling maneuver than control law A. This was achieved with less than a 2 percent increase in peak incremental bending moments relative to static load limits. This comparison demonstrates that the use of outboard leading-edge control surfaces may be more effective for reducing outboard torsion loads during rolling maneuvers than outboard trailing-edge controls while still significantly reducing inboard torsion loads with relatively little penalty from increases in incremental bending moments. These results confirm initial perceptions that only torsion moment need to be targeted for load reduction in designing an RMLA control law for this model.

It was demonstrated by experiment that the RMLA and flutter suppression control laws could be implemented simultaneously and operate effectively together during rolling maneuvers at dynamic pressures 11 percent above the open-loop flutter dynamic pressure.

NASA Langley Research Center
Hampton, VA 23681-0001
August 8, 1994

Appendix A

Aeroelastic Analysis and Parameter Identification

Equations of motion were developed during tests to have a state-space representation of AFW loads suitable for RMLA control law design and evaluation. System equations were defined by either equations (2), (4), or (5), depending upon how the pendulum term was included. The output equations were defined by equation (7). Equations were developed to model the plant at both $q = 150$ and 250 psf with experimental data to define the parameters in the linearized equations. For $q = 250$ psf, which is above the open-loop flutter dynamic pressure for the tip-ballast-coupled configuration, the experimental data were acquired only for the decoupled configuration. Time did not allow data for the coupled configuration to be obtained. Since decoupled data were the best that could be obtained for the higher dynamic pressure test condition prior to RMLA control law design, decoupled equations were used only to perform evaluations, not control law design. To be consistent with control law design for free-flying aircraft, and in light of the results of the study on the effect of mass eccentricity, the center of mass was assumed to be on the roll axis ($l = 0$) for the RMLA control law design. Since this assumption implies the pendulum term is 0, only the remaining linearized equations were used for the design models. Evaluation models included either the nonlinear or linear pendulum term. Test procedures used to acquire the necessary experimental data to identify the parameters in the linearized equations are identified below.

Data Acquisition

In order to identify the moment and load coefficients due to roll and roll rate, experimental data were acquired from rolling maneuvers in which control-surface deflections were 0, that is, by performing free-fall maneuvers of the AFW model at $q = 150$ and 250 psf. More specifically, at each dynamic pressure, the model was positioned at a roll angle of 90° with the roll-trim system (RTS). The model was then released (control surfaces were set to 0) and the model was allowed to return to its equilibrium position at or near a roll angle of 0° without control-surface actuation during the maneuver. The restoring force acting on the model was due solely to eccentricity of the model-mass c.g. below the roll axis.

Additional experimental load data were obtained during tests to determine the rolling and moment coefficients due to control-surface deflection by holding the model at a roll angle of 0° with the sting-mounted braking system, and then deflecting each control surface, δ_i, one at a time, at the rate of 5 deg/sec from 0 to 10°.

Damping-Coefficient Parameter Identification

With data obtained during the free-fall maneuvers, values for the parameters in the state-space equations were estimated in the following manner.

To determine the damping-in-roll element of $\mathbf{A}$, namely,

$$\frac{L_p}{I_{xx}}$$

equation (2) was used. Since all the $\delta_i = 0$ in free fall, and the pendulum term was defined for the model, the only undetermined value for these simulations was the damping-in-roll term. Consequently, analytical simulations of free fall were performed with this model in which the damping-in-roll coefficient was varied until the peak roll rate matched that observed in the test data. Figure 26(a) shows the actual free-fall experimental data at $q = 150$ psf with the final simulated curve superimposed.

Load Parameter Identification

Total loads during rolling maneuvers are defined by

$$\mathbf{y}_{\text{Load}} = \mathbf{C}_{\text{Load}}\mathbf{x} + \mathbf{D}_{\text{Load}}\mathbf{u} + \mathbf{E}_{\text{Load}} \tag{A1}$$

where

$$\mathbf{y}_{\text{Load}} = \left\{ M_{t_{\text{LI}}},\, M_{t_{\text{LO}}},\, M_{t_{\text{RI}}},\, M_{t_{\text{RO}}},\, M_{b_{\text{LI}}},\, M_{b_{\text{LO}}},\, M_{b_{\text{RI}}},\, M_{b_{\text{RO}}} \right\}^T$$

$$\mathbf{C}_{\text{Load}} = [\mathbf{C}_1 : \mathbf{C}_2]$$

$$\mathbf{C}_1 = \left\{ \frac{\partial M_\ell}{\partial \dot{\phi}} \right\}$$

$$\mathbf{C}_2 = \left\{ \frac{\partial M_\ell}{\partial \phi} \right\}$$

$$\ell = t_{\text{LI}},\, t_{\text{LO}},\, t_{\text{RI}},\, t_{\text{RO}},\, b_{\text{LI}},\, b_{\text{LO}},\, b_{\text{RI}},\, b_{\text{RO}}$$

Since there was no control-surface actuation during the free-fall maneuver, the load equations during these maneuvers are completely defined by the matrices $\mathbf{C}_{\text{Load}}$ and $\mathbf{E}_{\text{Load}}$ and can be determined from free-fall data. To identify elements of these matrices, it was first assumed that each load, M, acting on the model during roll could be described by the following linear equation,

$$M = \frac{\partial M}{\partial \dot{\phi}}\dot{\phi} + \frac{\partial M}{\partial \phi}\phi + M_0 \tag{A2}$$

Inertial loads were not modeled.

Next the elements of $\mathbf{E}_{\text{Load}}$, defined by the elements, M_0, were evaluated by averaging the total loads for short intervals of time after the model reached its equilibrium position when $\dot{\phi}$ and ϕ are both 0.

The elements of $\mathbf{C}_2$ in the partitioned matrix $\mathbf{C}_{\text{Load}}$ were determined by estimating the coefficient of ϕ in equation (A2) for each load M. This term results from the fact that a variation in steady-state loads existed in the data between the model at 90° and 0° roll angles. Since steady-state load values for roll-angle positions between 90° and 0° were not available, a straight line approximation was made so that the experimental models matched steady-state wind tunnel loads at 90° and 0° roll angles, and the partial of M with respect to ϕ was defined as the constant slope,

$$\frac{\partial M}{\partial \phi} = \frac{M_{90^\circ} - M_{0^\circ}}{90^\circ} \tag{A3}$$

The coefficient of $\dot{\phi}$ in equation (A2) defining the element of $\mathbf{C}_1$ corresponding to load M in the partitioned matrix $\mathbf{C}_{\text{Load}}$, was rewritten in terms of known quantities as follows:

$$\frac{\partial M}{\partial \dot{\phi}} = \frac{\left(M - \frac{\partial M}{\partial \phi}\phi - M_0 \right)}{\dot{\phi}} \tag{A4}$$

Each term in equation (A4) is a function of time; hence, division by the roll rate implies division by time-correlated values of the numerator and denominator. Because the acceleration is zero at the peak roll rate, it was assumed that the unmodeled inertial load would also be zero at this point because of its proportional relationship with acceleration. Thus, to obtain $\mathbf{C}_1$, the average

of equation (A4) is taken over a small interval of time corresponding to the occurrence of peak roll rate for each load. These averaged constant values define $\frac{\partial M}{\partial \dot{\phi}}$ for each load.

Rolling-Moment Coefficients Due to Control Surface Deflections

The elements of **B** describe the rolling moments due to control surface deflection. These values were identified from AFW static tests at the same tunnel conditions used in this study. Essentially, these values of the rolling moments per deflection angle were obtained from a load balance located in the sting to which the wind tunnel model was attached. During the static tests, several component moments and forces were measured from the balance as each control surface was statically deflected at various angles.

Load Coefficients Due to Control Surface Deflections

The elements of **D** are the loads due to control surface deflection. Load data obtained during tests with the model fixed at 0° roll angle were used to identify these elements. Loads were recorded for a 0° to 10° deflection at a rate of 5 deg/sec of each control surface as a function of time. The load data were then approximated with a straight line, and the slope was then divided by the 5 deg/sec rate of change of control surface position to obtain the change in load due to the change in control surface deflection,

$$\frac{\partial M}{\partial \delta_\ell} = \frac{\partial M}{\partial t} \div \frac{\partial \delta_\ell}{\partial t} \tag{A5}$$

Figures 26(a) through 26(j) compare time histories of roll rate, roll angle, and several loads generated during a free fall at $q = 150$ psf, with load generated during simulations by using equations (2) and (7) with parameters in **A**, **B**, **C**, **D**, and **E** defined as

$$\left.\begin{aligned}
\mathbf{A} &= \begin{bmatrix} -5.8 & 0 \\ 1.0 & 0 \end{bmatrix} \begin{matrix} \text{in-lb-sec/rad} \\ \text{in-lb/rad} \end{matrix} \\
\mathbf{B} &= \begin{bmatrix} -8.519 & 34.420 & 64.420 & 11.040 & -36.510 & -61.370 \\ 0 & 0 & 0 & 0 & 0 & 0 \end{bmatrix} \text{in-lb/rad} \\
\mathbf{C} &= \begin{bmatrix} 1 & 0 & -34.62 & -25.37 & -208.9 & 95.17 & -9.79 & 1.60 & 797.79 & 112.12 \\ 0 & 1 & -226.8 & 6.286 & -342.6 & 44.7 & 752.1 & 123.4 & 597.1 & 126.7 \end{bmatrix}^T \begin{matrix} \text{in-lb-sec/rad} \\ \text{in-lb/rad} \end{matrix} \\
\mathbf{D} &= \begin{bmatrix} 0 & 0 & 0 & 0 & 0 & 0 \\ 0 & 0 & 0 & 0 & 0 & 0 \\ -746.05 & -8417.37 & -9542.74 & 31.52 & 155.51 & -49.28 \\ -977.54 & -939.72 & -785.01 & 78.50 & 13.18 & 105.43 \\ 108.87 & 24.70 & 424.02 & -1009.63 & -11058.90 & -12176.25 \\ 56.73 & 110.02 & 56.14 & -863.51 & -185.65 & -390.21 \\ -2701.69 & 11339.67 & 15287.64 & -352.97 & 30.25 & 1719.00 \\ 267.02 & 3140.04 & 1104.17 & -9.05 & 21.49 & 128.35 \\ 287.65 & 813.66 & 706.51 & -2616.32 & 9912.90 & 14359.38 \\ 0.27 & 106.98 & 34.32 & 211.15 & 3730.23 & 1409.58 \end{bmatrix} \text{in-lb/rad} \\
\mathbf{E} &= [-1215.7 \quad 143.90 \quad -1223.1 \quad 267.60 \quad 4411.4 \quad 461.30 \quad 3657.0 \quad 566.20]^T \text{in-lb}
\end{aligned}\right\} \tag{A6}$$

The nonlinear pendulum term was included in these evaluations, and the simulations were performed with the Kutta-Merson method of solution. Simulated quantities are indicated by the smooth lines. Each curve approximates the mean of the experimental data fairly well over the time interval of interest. Flexible modes and noise were not modeled since they were not considered necessary for RMLA design; consequently, oscillations about the mean were not predicted. Similar comparisons were obtained for the model at $q = 250$ psf. The linear equation parameters for $q = 250$ psf are defined as

$$
\left.
\begin{aligned}
\mathbf{A} &= \begin{bmatrix} -7.25 & 0 \\ 1.0 & 0 \end{bmatrix} \begin{matrix} \text{in-lb-sec/rad} \\ \text{in-lb/rad} \end{matrix} \\
\mathbf{B} &= \begin{bmatrix} -25.40 & 17.80 & 70.70 & 25.40 & -17.70 & -70.70 \\ 0 & 0 & 0 & 0 & 0 & 0 \end{bmatrix} \text{in-lb/rad} \\
\mathbf{C} &= \begin{bmatrix} 1 & 0 & -83.43 & -26.19 & -376.6 & 105.3 & -198.5 & 20.2 & 964.4 & 165.8 \\ 0 & 1 & -209.6 & 7.11 & -393.2 & 48.6 & 840.0 & 131.0 & 576.4 & 134.2 \end{bmatrix}^T \begin{matrix} \text{in-lb-sec/rad} \\ \text{in-lb/rad} \end{matrix} \\
\mathbf{D} &= \begin{bmatrix}
0 & 0 & 0 & 0 & 0 & 0 \\
0 & 0 & 0 & 0 & 0 & 0 \\
-531.46 & -10\,801.62 & -14\,027.04 & 12.95 & 747.54 & -94.89 \\
-1879.67 & -2175.05 & -1900.64 & -3.53 & 13.40 & 134.25 \\
-34.57 & 237.39 & -327.01 & -844.95 & -12\,582.51 & -19\,258.53 \\
38.49 & 61.60 & 208.23 & -1572.71 & -1306.21 & -1192.41 \\
-6968.83 & 9974.21 & 19\,969.62 & -593.00 & -1527.04 & 4302.66 \\
-137.35 & 4291.77 & 1388.95 & -101.88 & -177.40 & 730.00 \\
326.04 & 153.28 & 1581.48 & -4136.95 & 10\,291.65 & 18\,753.14 \\
412.10 & -26.70 & 218.43 & 372.45 & 5410.84 & 1935.02
\end{bmatrix} \text{in-lb/rad} \\
\mathbf{E} &= [\,-1962.6 \quad 199.94 \quad -1883.6 \quad 408.69 \quad 6929.0 \quad 755.91 \quad 5812.4 \quad 903.66\,]^T \text{in-lb}
\end{aligned}
\right\} \qquad \text{(A7)}
$$

Design-Model Simulation Matrices

The coefficient matrices in equations (5) and (7), defining the design-model plant equations, are defined in equation (A6) for $q = 150$ psf and equation (A7) for $q = 250$ psf where

$$\mathbf{x} = \{\, \dot{\phi} \quad \phi \,\}^T$$

$$\mathbf{u} = \{\, \delta_{\mathrm{LEO_L}} \quad \delta_{\mathrm{TEO_L}} \quad \delta_{\mathrm{TEI_L}} \quad \delta_{\mathrm{LEO_R}} \quad \delta_{\mathrm{TEO_R}} \quad \delta_{\mathrm{TEI_R}} \,\}^T$$

$$\mathbf{y} = \{\, \dot{\phi} \quad \phi \quad M_{t_{\mathrm{LI}}} \quad M_{t_{\mathrm{LO}}} \quad M_{t_{\mathrm{RI}}} \quad M_{t_{\mathrm{RO}}} \quad M_{b_{\mathrm{LI}}} \quad M_{b_{\mathrm{LO}}} \quad M_{b_{\mathrm{RI}}} \quad M_{b_{\mathrm{RO}}} \,\}^T$$

Appendix B

Calculation of Mass Eccentricity Effects

Separating equation (1) into four moment contribution terms, the relative importance of each rolling moment contribution can be assessed. The four moment contributions are inertial rolling moment induced roll acceleration

$$M_{xx} = I_{xx}\ddot{\phi} \tag{B1}$$

the aerodynamic rolling moment induced by roll rate

$$M_p = L_p\dot{\phi} \tag{B2}$$

the pendulum rolling moment due to mass eccentricity

$$M_m = mgl\sin\phi \tag{B3}$$

and the aerodynamic rolling moment due to control surface deflections

$$M_\delta = \sum_{i=1}^{6} L_{\delta_i}\delta_i \tag{B4}$$

Initially, simulations used a preliminary set of equations to represent the AFW wind tunnel model described by equations (2a) and (2b) were performed with a control law structure that allowed all surfaces to be commanded by a single external ramp-hold input δ_c (i.e., each $\delta_i = \delta_c$). The control structure is illustrated in figure 8. Right and left control surfaces were deflected differentially. For individual control surfaces, it was assumed that downward deflection was positive. The convention for pairs of control surfaces used in the RMLA development and design was that a positive (differential) deflection caused the left control surface to be deflected upward and the right downward (positive). Different δ_c commands resulted in various time-to-roll-90° performance times t_F ranging in value from 0.5 sec to 3 sec. The parameters used in the equations of motion for this mass eccentricity study are defined in table B1. The roll angle $\phi(t)$ was determined from the simulation by using the variable step Kutta-Merson method, and each of the terms defined by equations (B1) through (B4) were plotted. Figure 9 shows the results of two of these simulations at $q = 150$ psf for two different performance times. Figures 9(a) and (9c) show the time histories of the roll angle and roll rate, ϕ and $\dot{\phi}$, in terms of degrees and deg/sec, respectively. Figures 9(b) and (9d) show M_{xx}, M_p, M_m, and M_δ for each t_F, respectively. The performance time to roll from 90° to 0° for figures 9(a) and (9b) is $t_F = 0.58$ sec, as indicated in figure 9(a). For figures 9(c) and (9d), $t_F = 1.8$ sec, as indicated in figure 9(c). By comparing the magnitudes of M_m, and M_δ for $0 < t < t_F$, for each t_F, it can be seen that $|M_m|$ is small relative to $|M_\delta|$ during the faster rolling maneuver ($t_F = 0.58$ sec) once the control surfaces are deflected. However, $|M_m|$ is significantly larger relative to $|M_\delta|$ during the slower rolling maneuver ($t_F = 1.8$ sec). In fact, $|M_m|$ is larger than $|M_\delta|$ during the first 1.2 sec.

To better quantify the total pendulum effect, integrals of the magnitudes of the pendulum rolling moment and the aerodynamic rolling moment were generated as functions of the time required to roll from 90° to 0°.

$$\mathcal{M}_m = \int_{t=0}^{t=t_F} |M_m|dt = \int_{t=0}^{t=t_F} |mgl\sin\phi(t)|dt \tag{B5}$$

and

$$\mathcal{M}_\delta = \int_{t=0}^{t=t_F} |M_\delta| dt = \int_{t=0}^{t=t_F} \left| \sum_{i=1}^{6} L_{\delta_i} \delta_i \right| dt \tag{B6}$$

Figure 10 shows the results of these integral calculations over a range of performance times from 0.5 to 3 sec for the same model described above at $q = 150$ psf in which the δ_i were control surface commands that achieved the specified times to roll. The points corresponding to $t_F = 0.58$ sec and $t_F = 1.8$ sec are identified on the plot. It can be seen that $\mathcal{M}_m$ is small relative to $\mathcal{M}_\delta$ during fast rolling maneuvers ($t_F < 1$ sec); however, $\mathcal{M}_m$ is large relative to $\mathcal{M}_\delta$ during slow rolling maneuvers ($t_F > 1$ sec), which provides a significant restoring force that aids the rolling maneuver.

This same trend in relative sizes of $\mathcal{M}_m$ and $\mathcal{M}_\delta$ could be seen in simulations at other dynamic pressures and other combinations of control surface deflections, including closed-loop simulations. Rolling faster reduces the contribution of the pendulum rolling moment to the total rolling moment relative to the aerodynamic rolling moment due to control surface deflections.

Table B1. Mass Eccentricity Simulation Model

mgl, lb-in	1329.5
I_{xx}, lb-in-sec^2	256.9
L_p, lb-in-sec	1184.4
$L_{\delta_{\mathrm{LEO,L}}}$, lb-in/deg	−2188
$L_{\delta_{\mathrm{TEO,L}}}$, lb-in/deg	8841
$L_{\delta_{\mathrm{TEI,L}}}$, lb-in/deg	16501
$L_{\delta_{\mathrm{LEO,R}}}$, lb-in/deg	2836
$L_{\delta_{\mathrm{TEO,R}}}$, lb-in/deg	−9378
$L_{\delta_{\mathrm{TEI,R}}}$, lb-in/deg	−15764
M_δ, lb-in-sec, at—	
$t_F = 0.58$ sec	2.34
$t_F = 0.96$ sec	1.54
$t_F = 1.80$ sec	0.724
M_m, lb-in-sec, at—	
$t_F = 0.58$ sec	0.567
$t_F = 0.96$ sec	0.884
$t_F = 1.80$ sec	1.425

References

1. O'Connell, R. F.: Design, Development and Implementation of an Active Control System for Load Alleviation for a Commercial Transport Airplane. AGARD-R-683, Feb. 1980. (Available from DTIC as AD A082 959.)

2. Rollwagen, G.; Ellgoth, H.; and Beuck, G.: Identification of Dynamic Response, Simulation and Design of a Highly Nonlinear Digital Load Alleviation System for a Modern Transport Aircraft. *ICAS Proceedings—1990*, Sept. 1990, pp. 427–433. (Available as ICAS-90-1.3.4.)

3. Sandford, Maynard C.; Abel, Irving; and Gray, David L.: *Development and Demonstration of a Flutter-Suppression System Using Active Controls.* NASA TR R-450, 1975.

4. Noll, T. E.; and Huttsell, L. J.: Wing Store Active Flutter Suppression—Correlation of Analyses and Wind-Tunnel Data. *J. Aircr.*, vol. 16, no. 7, July 1979, pp. 491–497.

5. Roger, Kenneth L.; Hodges, Garold E.; and Felt, Larry: Active Flutter Suppression—A Flight Test Demonstration. *J. Aircr.*, vol. 12, no. 6, June 1975, pp. 551–556.

6. Sensburg, O.; Honlinger, H.; Noll, T. E.; and Huttsell, L. J.: Active Flutter Suppression on an F-4F Aircraft. *J. Aircr.*, vol. 19, no. 5, May 1982, pp. 354–359.

7. Miller, Gerald D.: *Active Flexible Wing (AFW) Technology.* AFWAL-TR-87-3096, U.S. Air Force, Feb. 1988. (Available from DTIC as AD B131 204.)

8. Perry, Boyd, III; Cole, Stanley R.; and Miller, Gerald D.: A Summary of the Active Flexible Wing Program. *A Collection of Technical Papers—AIAA Dynamics Specialist Conference,* Apr. 1992, pp. 1–10. (Available as AIAA-92-2080-CP and NASA TM-107655.)

9. Reed, Wilmer H., III; Foughner, Jerome T., Jr.; and Runyan, Harry L., Jr.: Decoupler Pylon: A Simple, Effective Wing/Store Flutter Suppressor. *J. Aircr.*, vol. 17, no. 3, Mar. 1980, pp. 206–211.

10. Hoadley, S. T.; and McGraw, S. M.: The Multi-Input/Multi-Output Multi-Function Digital Controller System for the AFW Wind-Tunnel Model. *A Collection of Technical Papers—AIAA Dynamics Specialists Conference*, Apr. 1992, pp. 30–38. (Available as AIAA-92-2083 and NASA TM-107600.)

11. Perry, Boyd, III; Dunn, H. J.; and Sandford, Maynard C.: Control Law Parameterization for an Aeroelastic Wind-Tunnel Model Equipped With an Active Roll Control System and Comparison With Experiment. A Collection of Technical Papers, Part 1—AIAA/ASME/ASCE/AHS 29th Structure, Structural Dynamics and Materials Conference, Apr. 1988, pp. 41–56. (Available as AIAA-88-2211.)

12. Etkin, Bernard: *Dynamics of Flight.* John Wiley & Sons, Inc., 1959.

13. MATRIX_x/SystemBuild User's Guide. Version 2.04X, Integrated Systems, Inc., 1990.

14. Mukhopadhyay, V.; and Newsom, J. R.: A Multi-loop System Stability Margin Study Using Matrix Singular Values. *J. Guid., Control, & Dyn.*, vol. 7, no. 5, Sept.–Oct. 1984, pp. 582–587.

15. Yates, E. Carson, Jr.; Land, Norman S.; and Foughner, Jerome T., Jr.: *Measured and Calculated Subsonic and Transonic Flutter Characteristics of a 45° Sweptback Wing Planform in Air and in Freon-12 in the Langley Transonic Dynamics Tunnel.* NASA TN D-1616, 1963.

16. Mukhopadhyay, Vivek: Flutter Suppression Digital Control Law Design and Testing for the AFW Wind-Tunnel Model. *A Collection of Technical Papers—AIAA Dynamics Specialist Conference,* Apr. 1992, pp. 156–161. (Available as AIAA-92-2095-CP.)

Table 1. Load Effectiveness Trends

δ_{TEI}, deg	δ_{TEO}, deg	δ_{LEO}, deg	$M_{b_{\mathrm{O}}}$	$M_{b_{\mathrm{I}}}$	$M_{t_{\mathrm{O}}}$	$M_{t_{\mathrm{I}}}$
6.4	2		Increase	Increase	Increase	Increase
8.7	−2		Decrease	Decrease	Decrease	Decrease
7.9		2	Increase	Increase		Increase
7.3		−2	Decrease	Decrease	Increase	Decrease

Table 2. Control Law Gains at $q = 150$ psf

Gains	Control law A	Control law B	Baseline
K_{com}	0.3500	0.3000	0.3500
K_{TEI}	−.0625	−.0667	−.0500
K_{TEO}	−.0384	0	0
K_{LEO}	0	.0356	0

Table 3. Eigenvalues of Closed-Loop Systems

Control law	$q = 150$ psf		$q = 250$ psf	
	Real	Imaginary	Real	Imaginary
A	−0.327	0	−0.176	0
	−1.606	0	−2.954	0
B	−0.358	0	−0.286	0
	−1.453	0	−1.820	0

Table 4. Test Conditions for Single-Function Open-Loop Tests With Control Laws A and B

q, psf	Mach	Tip ballast	Flutter suppression
150	0.33	Coupled	Off
200	.38	Coupled	Off
250	.44	Decoupled	Off

Table 5. Test Conditions for Multiple-Function Tests With Control Law B

q, psf	Mach	Tip ballast	Flutter suppression
250	0.44	Coupled	On
260	.45	Coupled	On

Table 6. Steady-State Loads at Start of Rolling Maneuvers (90°)

Dynamic pressure, psf	Wing	TMO, in-lb	TMI, in-lb	BMO, in-lb	BMI, in-lb
150	Left	69.6	−1932.9	800.8	6207.3
	Right	377.3	−1261.1	789.9	4555.3
	Average magnitude	223.4	1597.0	795.4	5381.3
200	Left	54.5	−2378.7	964.2	7394.6
	Right	415.0	−1585.1	948.7	5434.0
	Average magnitude	234.8	1981.9	956.5	6414.3
250	Left	40.4	−2712.3	1052.2	8401.5
	Right	469.7	−2016.0	1155.1	6322.4
	Average magnitude	255.1	2364.2	1103.7	7362.0

Table 7. Static Load Limits

Wing	Load limits for—			
	TMO, in-lb	TMI, in-lb	BMO, in-lb	BMI, in-lb
Left	1627.0	8929.0	4099.0	20 965.0
Right	1425.0	9434.0	3546.0	18 084.0
Minimum	1425.0	8929.0	3546.0	18 084.0

Table 8. Percent Change in Peak Incremental Loads Relative to Baseline Load Limits for Control Laws Having Nearly the Same Performance Time at $q = 200$ psf

	Time to roll 90°, sec	Peak incremental loads for—			
		TMO, in-lb	TMI, in-lb	BMO, in-lb	BMI, in-lb
Baseline	0.65	495.1	1565.0	185.7	352.2
RMLA A	0.66	359.6	747.1	638.0	403.8
Percent change from baseline		−27.4	−52.3	243.6	14.7
RMLA B	0.645	265.6	885.8	259.5	408.6
Percent change from baseline		−46.4	−43.4	39.7	16.0

Table 9. Percent Change in Peak Incremental Loads Relative to Minimum Static Load Limits for Control Laws Having Nearly the Same Performance Time at $q = 200$ psf

	Time to roll 90°, sec	Peak incremental loads for—			
		TMO, in-lb	TMI, in-lb	BMO, in-lb	BMI, in-lb
Baseline	0.65	495.1	1565.0	185.7	352.2
RMLA A	0.66	359.6	747.1	638.0	403.8
Percent change relative to limit		−9.5	−9.2	12.8	0.3
RMLA B	0.645	265.6	885.8	259.5	408.6
Percent change relative to limit		−16.1	−7.6	2.1	0.3

Table 10. Peak Incremental Loads From Experimental Data for Baseline

Dynamic pressure, psf	Control law	Time to roll 90°, sec	Peak incremental loads for—			
			TMO, in-lb	TMI, in-lb	BMO, in-lb	BMI, in-lb
150	Baseline	0.670	391.6	1206.0	180.9	313.6
150	Baseline	.705	343.7	1102.0	164.9	342.2
150	Baseline	.825	304.3	988.9	118.1	413.0
200	Baseline	0.575	580.0	1829.0	282.1	423.3
200	Baseline	.650	495.1	1565.0	185.7	352.2
200	Baseline	.805	394.1	1256.0	130.8	459.9
250	Baseline	0.555	719.1	2239.0	312.5	414.7
250	Baseline	.645	636.2	1803.0	269.0	363.1
250	Baseline	.665	544.4	1617.0	244.8	460.4
250	Baseline	.795	506.7	1497.0	168.4	429.1
150	A	0.675	308.4	679.5	493.8	313.3
150	A	.695	300.7	699.5	488.4	361.8
150	A	.805	263.4	523.2	415.4	279.2
200	A	0.635	376.3	628.5	731.1	442.7
200	A	.660	359.6	747.1	638.0	403.8
200	A	.770	302.1	570.6	551.3	341.2
250	A	0.600	405.0	776.0	915.4	560.0
250	A	.640	394.4	741.1	825.2	590.6
250	A	.735	335.2	615.9	696.8	486.6
150	B	0.650	251.1	858.1	250.8	334.6
150	B	.675	225.6	787.2	234.4	307.6
150	B	.780	178.0	684.7	164.8	455.7
200	B	0.615	279.0	1064.0	294.3	450.1
200	B	.645	265.6	885.8	259.5	408.6
200	B	.740	205.1	772.9	217.7	547.3
250	B	0.630	293.4	909.1	328.0	366.2
250	B	.740	218.0	821.1	230.1	498.4
250	B	.770	226.4	700.4	240.5	531.0

Table 11. Peak Incremental Loads for RMLA Control Laws With Interpolated Baseline Maneuver Loads

(a) RMLA control law A

Dynamic pressure, psf	Time to roll 90°, sec	Peak incremental loads for—							
		TMO, in-lb		TMI, in-lb		BMO, in-lb		BMI, in-lb	
		Baseline[a]	Control A	Baseline[a]	Control A	Baseline[a]	Control A	Baseline[a]	Control A
150	0.675	384.8	308.4	1191.1	679.5	178.6	493.8	317.7	313.3
150	.695	357.4	300.7	1131.7	699.5	169.5	488.4	334.0	361.8
150	.805	310.9	263.4	1007.8	523.2	125.9	415.4	401.2	279.2
200	0.635	512.1	376.3	1617.8	628.5	205.0	731.1	366.4	442.7
200	.660	488.6	359.6	1545.1	747.1	182.2	638.0	359.1	403.8
200	.770	416.9	302.1	1325.8	570.6	143.2	551.3	435.6	341.2
250	0.600	677.7	405.0	2021.0	776.0	290.8	915.4	388.9	560.0
250	.640	640.8	394.4	1827.2	741.1	271.4	825.2	366.0	590.6
250	.735	524.1	335.2	1552.4	615.9	203.7	696.8	443.5	486.6

(b) RMLA control law B

Dynamic pressure, psf	Time to roll 90°, sec	Peak incremental loads for—							
		TMO, in-lb		TMI, in-lb		BMO, in-lb		BMI, in-lb	
		Baseline[a]	Control B	Baseline[a]	Control B	Baseline[a]	Control B	Baseline[a]	Control B
150	0.650	419.0	251.1	1265.4	858.1	190.0	250.8	297.3	334.6
150	.675	384.8	225.6	1191.1	787.2	178.6	234.4	317.7	307.6
150	.780	319.1	178.0	1031.3	684.7	135.7	164.8	386.5	455.7
200	0.615	534.7	279.0	1688.2	1064.0	230.7	294.3	385.4	450.1
200	.645	500.8	265.6	1582.6	885.8	192.1	259.5	356.9	408.6
200	.740	436.5	205.1	1385.6	772.9	153.8	217.7	414.7	547.3
250	0.630	650.0	293.4	1875.7	909.1	276.2	328.0	371.7	366.2
250	.740	522.7	218.0	1547.8	821.1	200.7	230.1	442.3	498.4
250	.770	514.0	226.4	1520.1	700.4	183.1	240.5	435.1	531.0

[a]Interpolated.

Table 12. Percent Change in Peak Incremental Load Between Baseline and RMLA-Controlled Loads Relative to Baseline Loads, Initial Steady-State Loads, and Minimum Static Load Limit

Control law	Dynamic pressure, psf	Time to roll 90°, sec	TMO relative to—			TMI relative to—			BMO relative to—			
			Peak incremental baseline load, percent	Initial steady-state load, percent	Miminum static load limit, percent	Peak incremental baseline load, percent	Initial steady-state load, percent	Miminum static load limit, percent	Peak incremental baseline load, percent	Initial steady-state load, percent	Miminum static load limit, percent	Pea increme baseline perce
A	150	0.675	−19.8	−34.2	−5.4	−43.0	−32.0	−5.7	176.5	39.6	8.9	1
A	150	.695	−15.9	−25.4	−4.0	−38.2	−27.1	−4.8	188.2	40.1	9.0	−8
A	150	.805	−15.3	−21.2	−3.3	−48.1	−30.3	−5.4	229.9	36.4	8.2	30
A	200	0.635	−26.5	−57.8	−9.5	−61.2	−49.9	−11.1	256.7	55.0	14.8	−20
A[a]	200	.660	−26.4	−54.9	−9.1	−51.6	−40.3	−8.9	250.2	47.7	12.9	−12
A	200	.770	−27.5	−48.9	−8.1	−57.0	−38.1	−8.5	285.0	42.7	11.5	21
A	250	0.600	−40.2	−106.9	−19.1	−61.6	−52.7	−13.9	214.8	56.6	17.6	−44
A	250	.640	−38.5	−96.6	−17.3	−59.4	−45.9	−12.2	204.0	50.2	15.6	−61
A	250	.735	−36.0	−74.1	−13.3	−60.3	−39.6	−10.5	242.1	44.7	13.9	−9
B	150	0.650	−40.1	−75.1	−11.8	−32.2	−25.5	−4.6	32.0	7.6	1.7	−12
B	150	.675	−41.4	−71.2	−11.2	−33.9	−25.3	−4.5	31.2	7.0	1.6	3
B	150	.780	−44.2	−63.1	−9.9	−33.6	−21.7	−3.9	21.5	3.7	.8	−17
B	200	0.615	−47.8	−108.9	−17.9	−37.0	−31.5	−7.0	27.6	6.7	1.8	−16
B[a]	200	.645	−47.0	−100.2	−16.5	−44.0	−35.2	−7.8	35.1	7.0	1.9	−14
B	200	.740	−53.0	−98.6	−16.2	−44.2	−30.9	−6.9	41.5	6.7	1.8	−32
B	250	0.630	−54.9	−139.8	−25.0	−51.5	−40.9	−10.8	18.7	4.7	1.5	1
B	250	.740	−58.3	−119.4	−21.4	−46.9	−30.7	−8.1	14.6	2.7	.8	−12
B	250	.770	−55.9	−112.7	−20.2	−53.9	−34.7	−9.2	31.4	5.2	1.6	−22

[a] Interpolated.

Table 13. Percent Loads Relative to Minimum Static Load Limits for RMLA-Controlled, Baseline, and Initial Steady-State Loads

Control law	Dynamic pressure, psf	Time to roll 90°, sec	Load, percent, for—									
			TMO			TMI			BMO			
			Baseline	RMLA	Initial	Baseline	RMLA	Initial	Baseline	RMLA	Initial	Bas
A	150	0.675	27.0	21.6	15.7	13.3	7.6	17.9	5.0	13.9	22.4	
A	150	.695	25.1	21.1	15.7	12.7	7.8	17.9	4.8	13.8	22.4	
A	150	.805	21.8	18.5	15.7	11.3	5.9	17.9	3.6	11.7	22.4	
A	200	0.635	35.9	26.4	16.5	18.1	7.0	22.2	5.8	20.6	27.0	
A	200	.660	34.3	25.2	16.5	17.3	8.4	22.2	5.1	18.0	27.0	
A	200	.770	29.3	21.2	16.5	14.8	6.4	22.2	4.0	15.5	27.0	
A	250	0.600	47.6	28.4	17.9	22.6	8.7	26.5	8.2	25.8	31.1	
A	250	.640	45.0	27.7	17.9	20.5	8.3	26.5	7.7	23.3	31.1	
A	250	.735	36.8	23.5	17.9	17.4	6.9	26.5	5.7	19.7	31.1	
B	150	0.650	29.4	17.6	15.7	14.2	9.6	17.9	5.4	7.1	22.4	
B	150	.675	27.0	15.8	15.7	13.3	8.8	17.9	5.0	6.6	22.4	
B	150	.780	22.4	12.5	15.7	11.6	7.7	17.9	3.8	4.6	22.4	
B	200	0.615	37.5	19.6	16.5	18.9	11.9	22.2	6.5	8.3	27.0	
B	200	.645	35.1	18.6	16.5	17.7	9.9	22.2	5.4	7.3	27.0	
B	200	.740	30.6	14.4	16.5	15.5	8.7	22.2	4.3	6.1	27.0	
B	250	0.630	45.6	20.6	17.9	21.0	10.2	26.5	7.8	9.2	31.1	
B	250	.740	36.7	15.3	17.9	17.3	9.2	26.5	5.7	6.5	31.1	
B	250	.770	36.1	15.9	17.9	17.0	7.8	26.5	5.2	6.8	31.1	

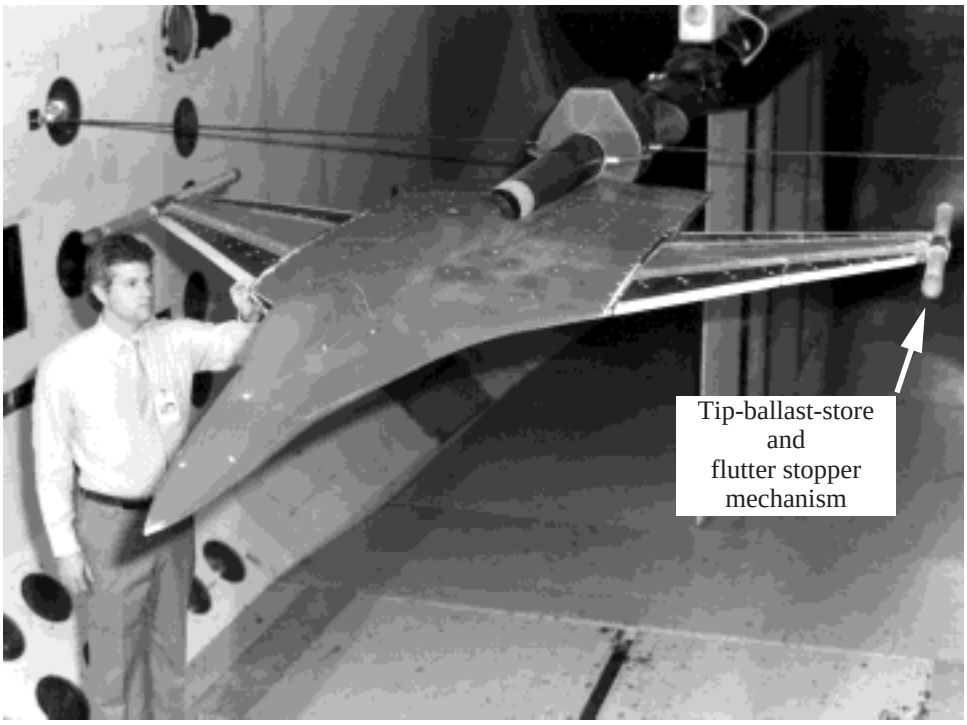

L-89-12442

(a) AFW model mounted in the Langley TDT prior to tests.

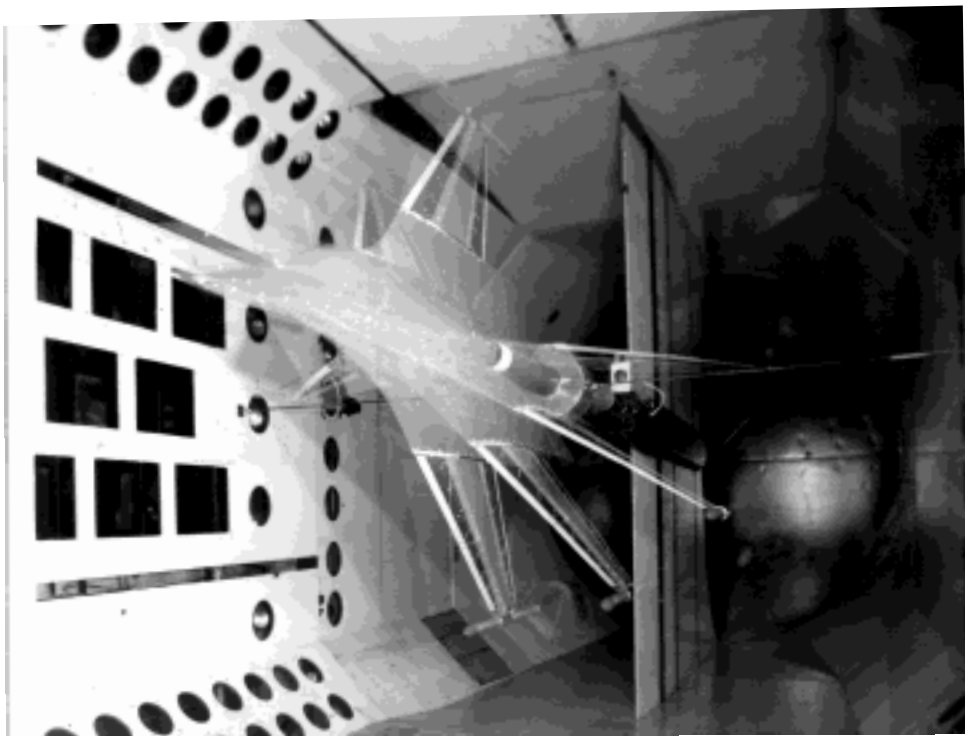

L-89-12446

(b) Multiple-exposure photograph showing the model at four different roll positions.

Figure 1. Photographs of the AFW model modified for the 1989 and 1991 wind tunnel tests and mounted in the Langley Transonic Dynamics Tunnel.

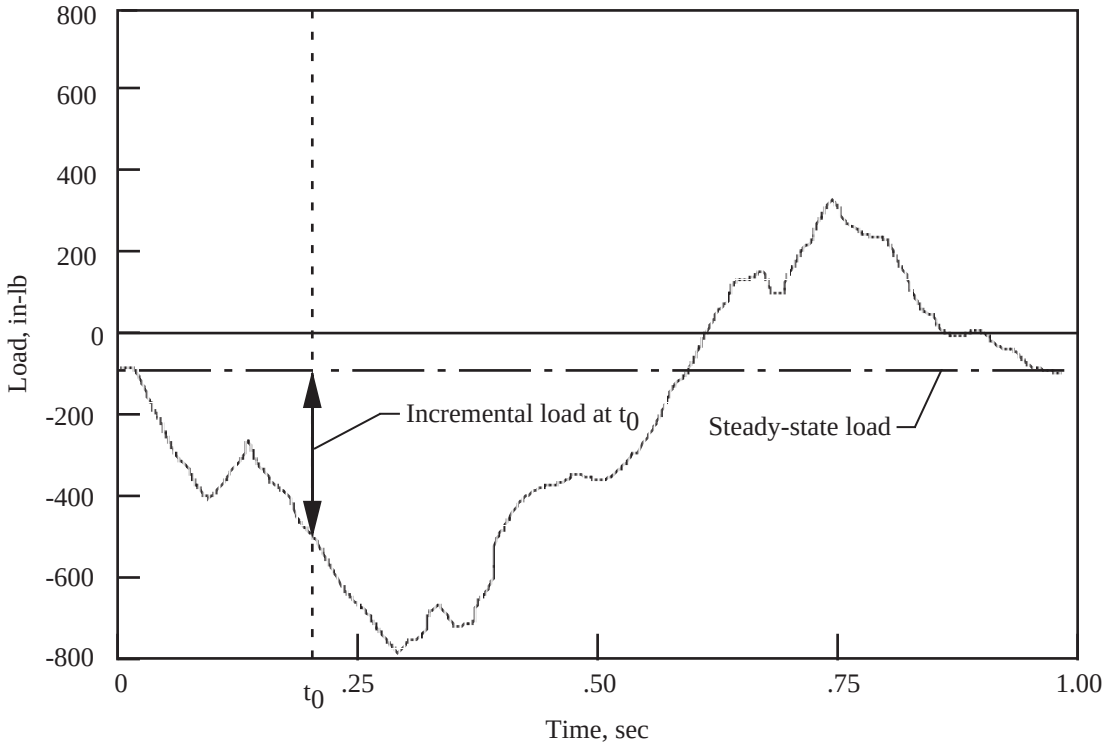

(a) Load during rolling maneuver.

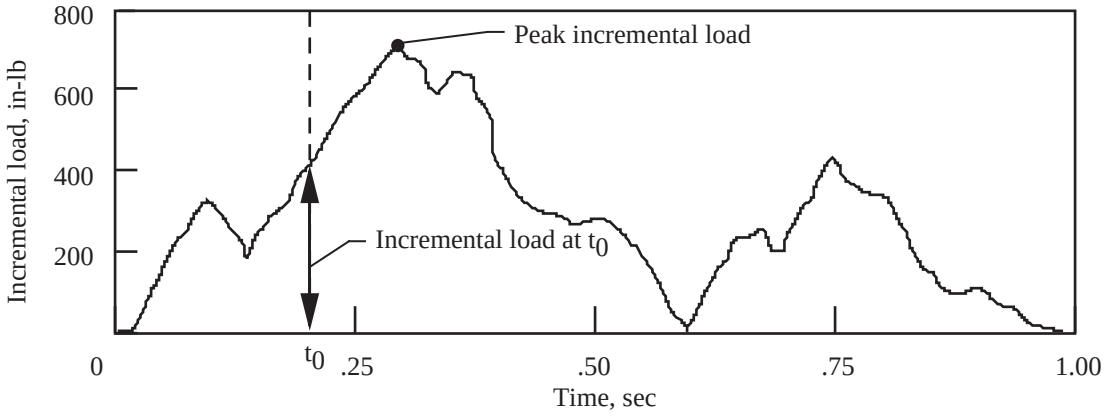

(b) Incremental load during rolling maneuver.

Figure 2. Wing-load time history illustrating incremental load.

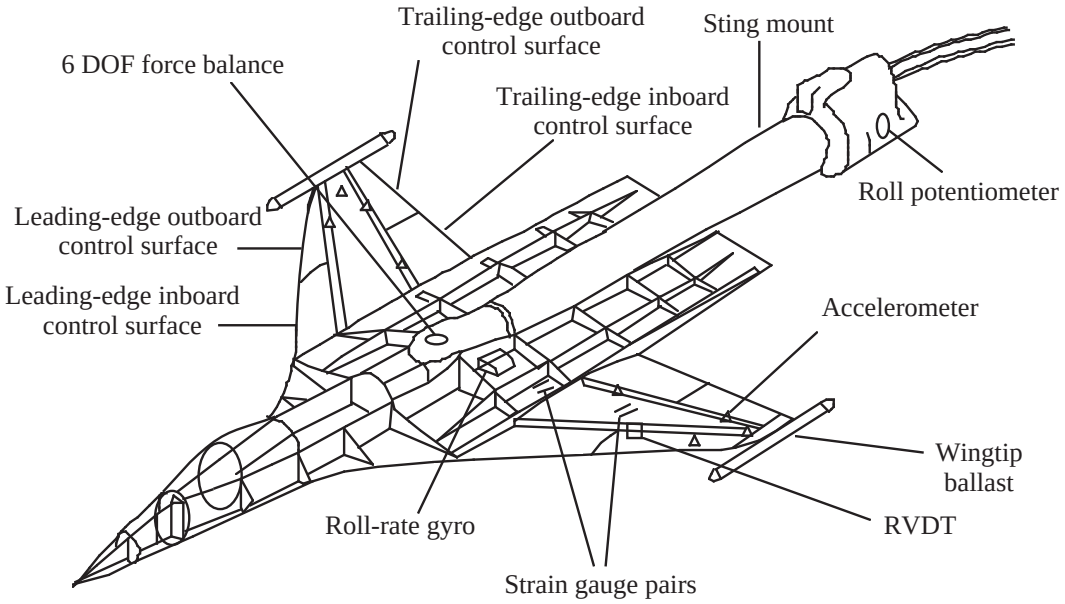

(a) AFW model control surface locations and instrumentation.

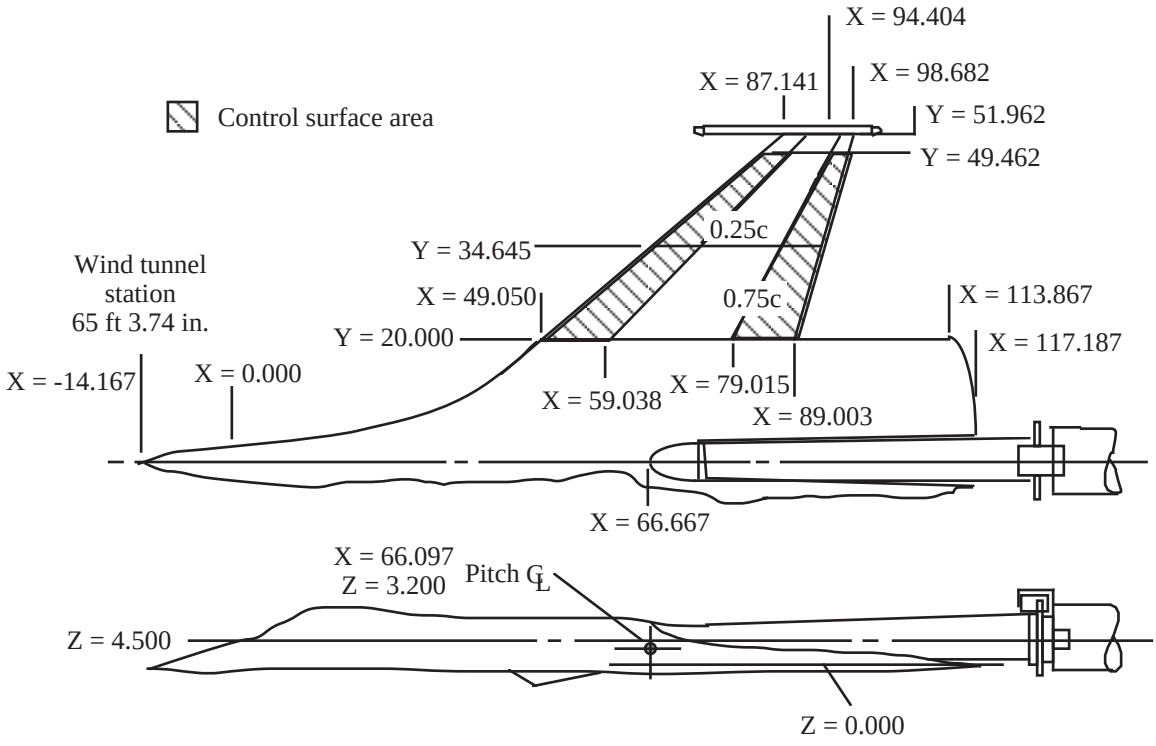

(b) Physical dimensions of AFW model with control surfaces delineated.

Figure 3. Schematics of AFW model control surface locations and instrumentation. All dimensions are in inches unless otherwise specified.

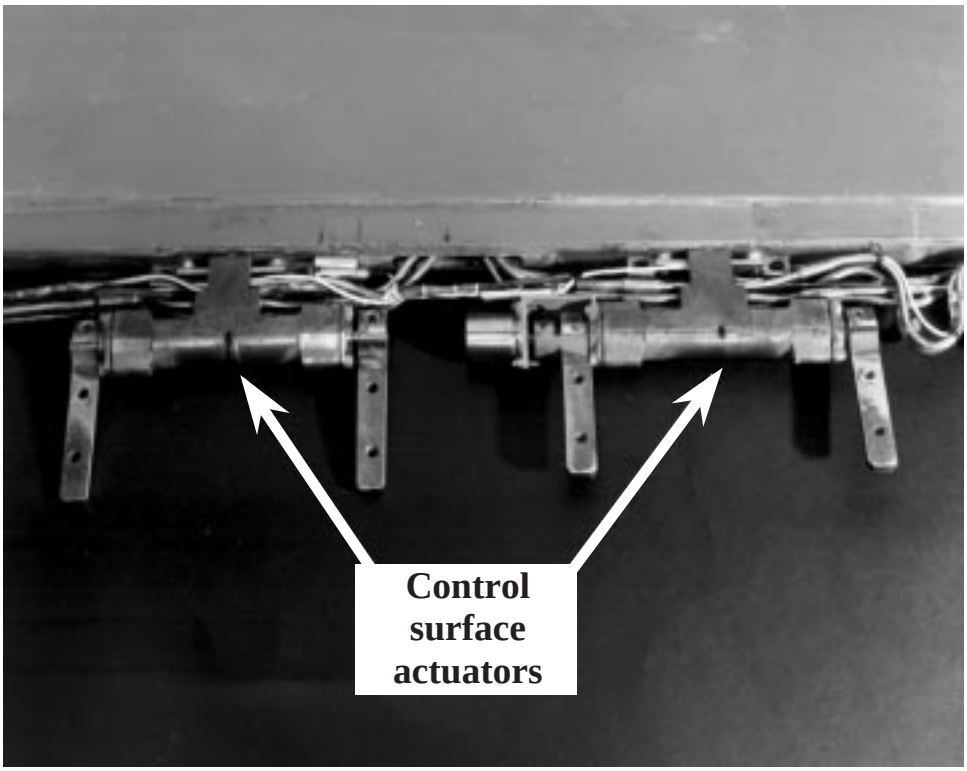

L-90-12024

Figure 4. Photograph of actuator and attachment to wing.

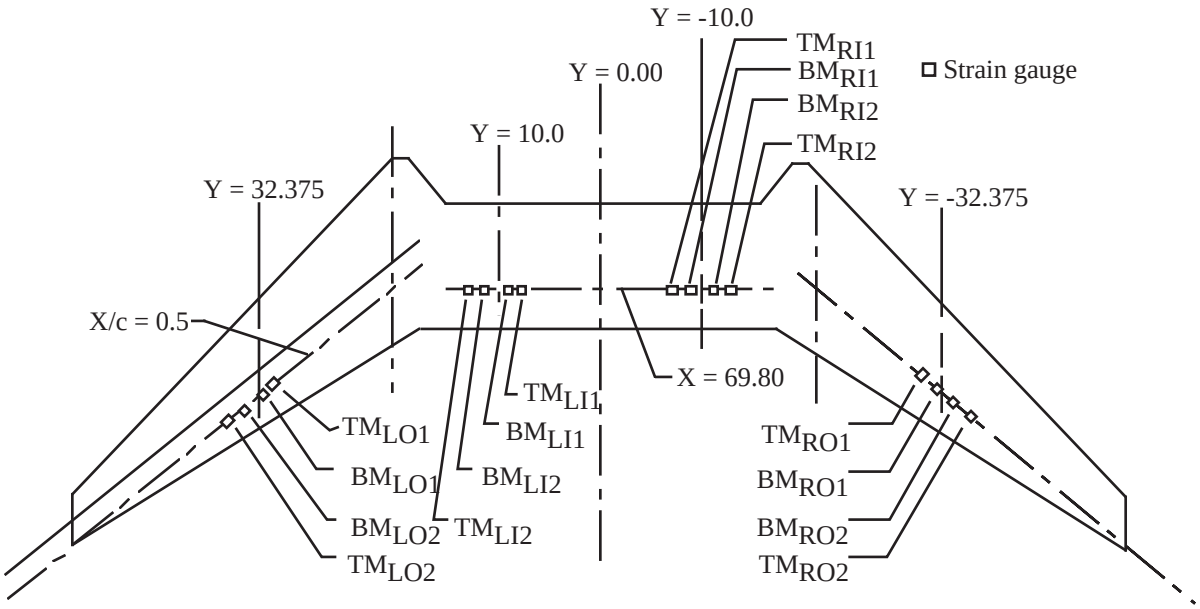

Figure 5. AFW strain gauge locations. All dimensions are in inches. (From ref. 7.)

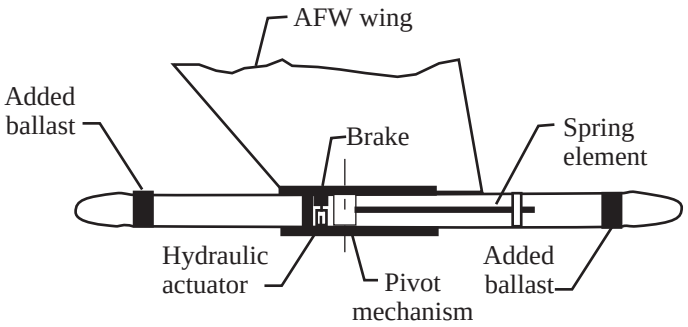

Figure 6. Tip-ballast decoupler pylon.

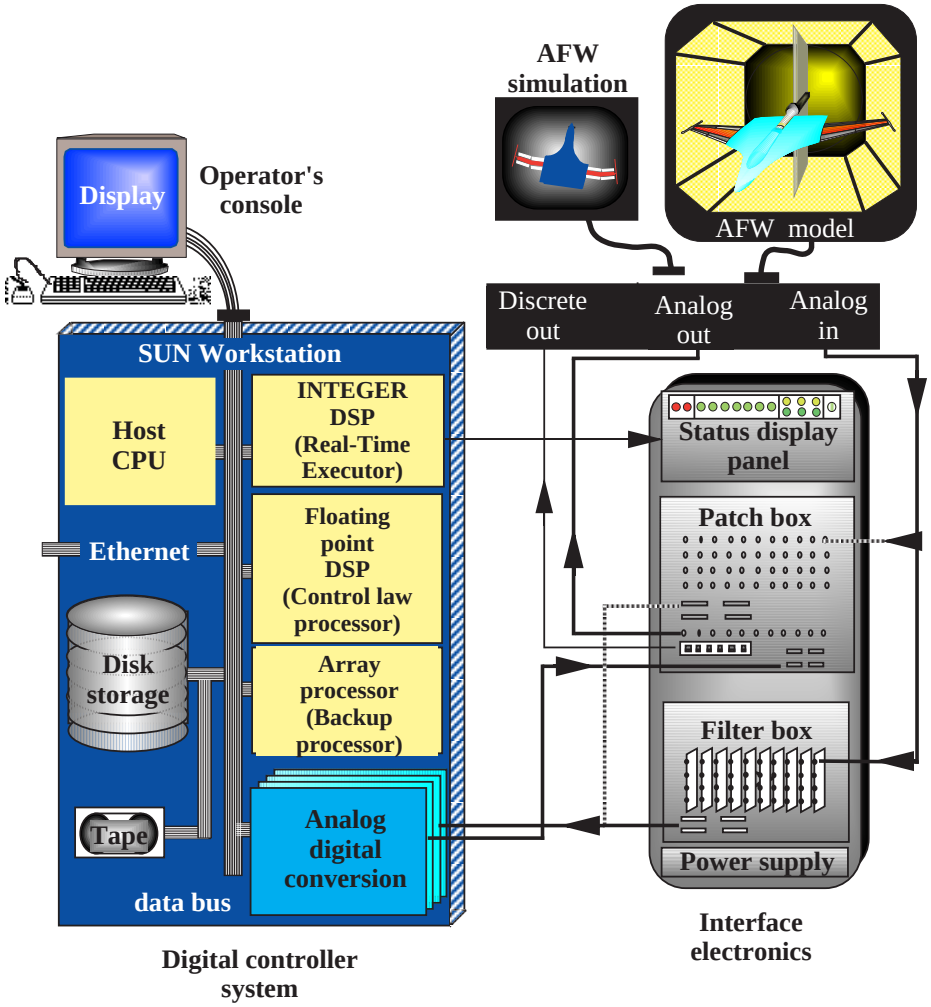

Figure 7. Schematic of AFW digital controller.

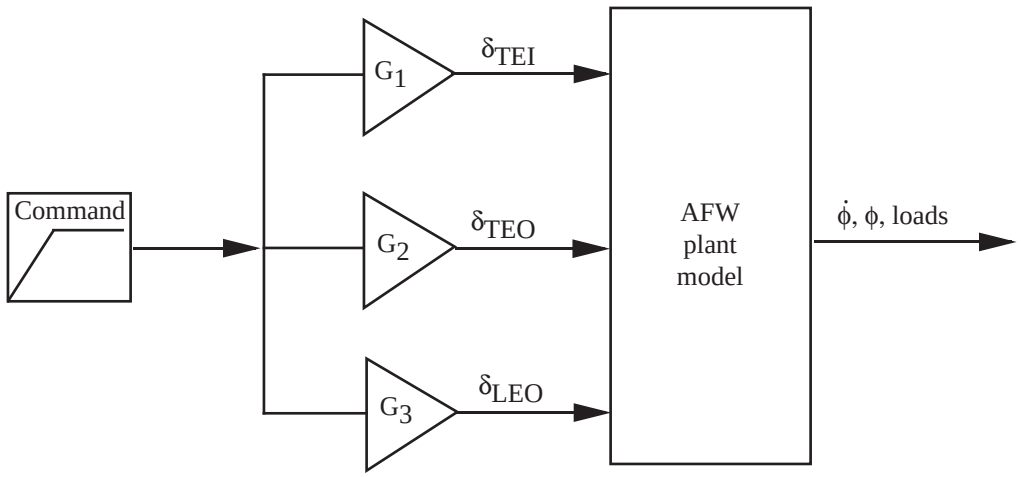

Figure 8. Analysis structure for load effectiveness study.

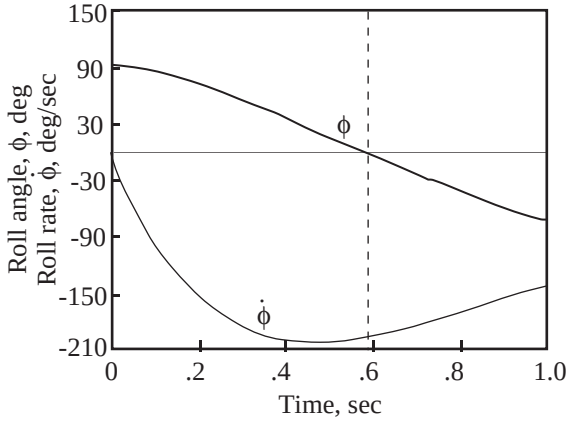

(a) $t_F = 0.58$ sec.

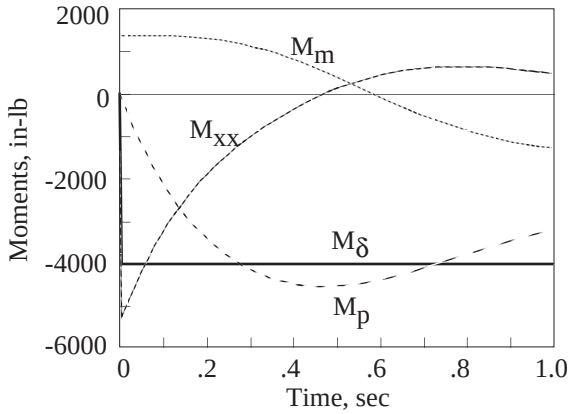

(b) Moment contributions for time to roll 90° of $t_F = 0.58$ sec.

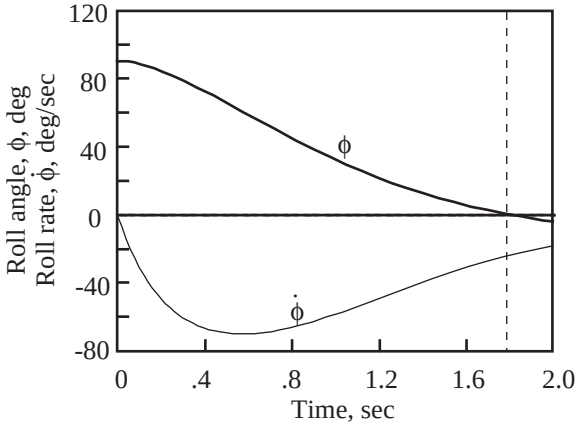

(c) $t_F = 1.8$ sec.

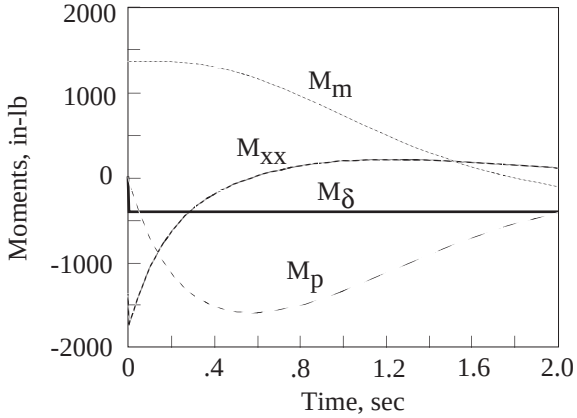

(d) Moment contributions for time to roll 90° of $t_F = 1.8$ sec.

Figure 9. Simulated roll angle, roll rate, and moments for $q = 150$ psf with mass eccentricity.

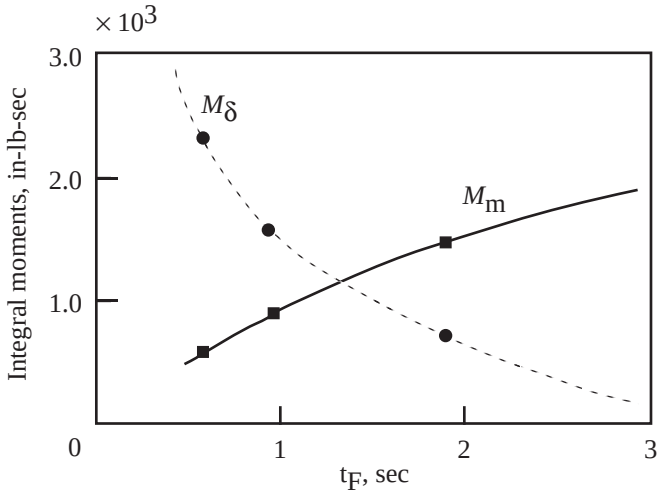

Figure 10. Simulated pendulum rolling moment and control-surface rolling moment integral values at $q = 150$ psf.

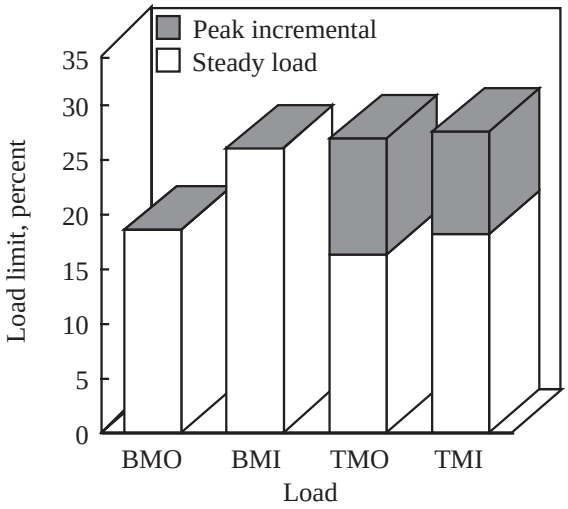

Figure 11. Design model steady load plus peak incremental load.

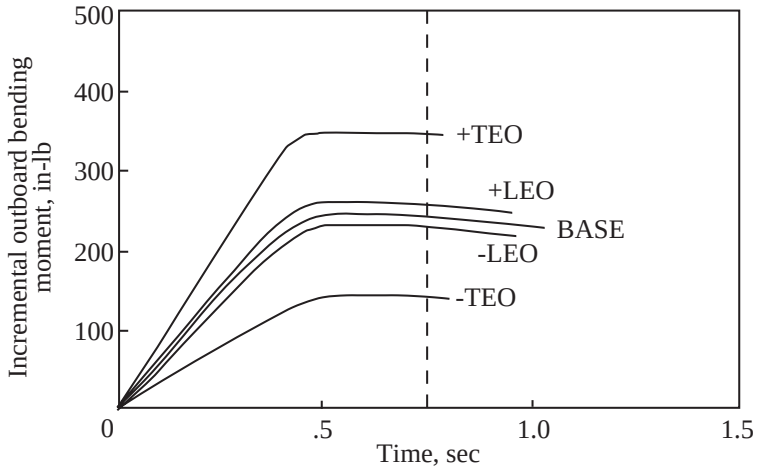

Figure 12. Incremental outboard bending moment generated during rolling maneuvers.

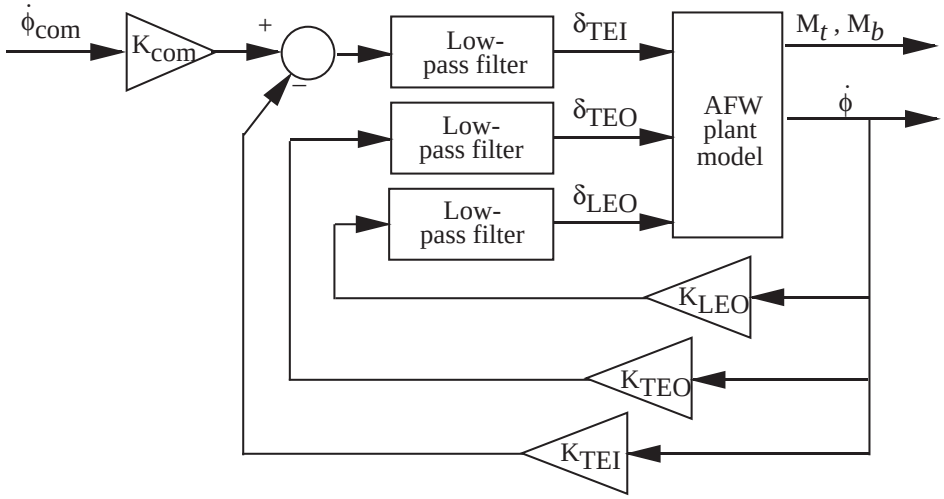

Figure 13. RMLA control law structure.

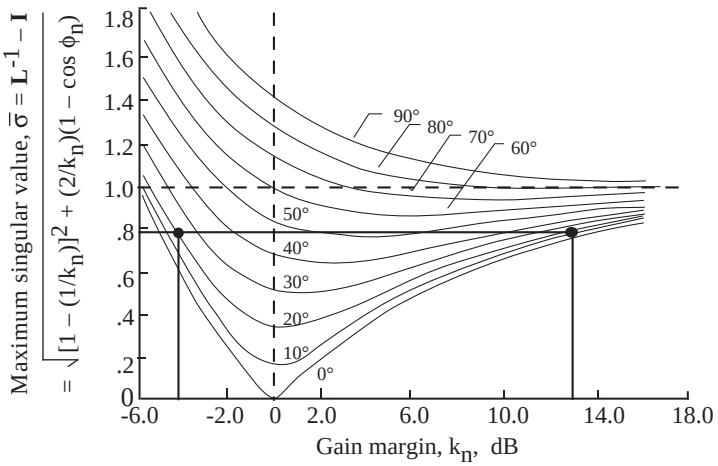

Figure 14. Universal diagram for multiloop gain-phase margin evaluation. (Based on fig. 2 from ref. 14.)

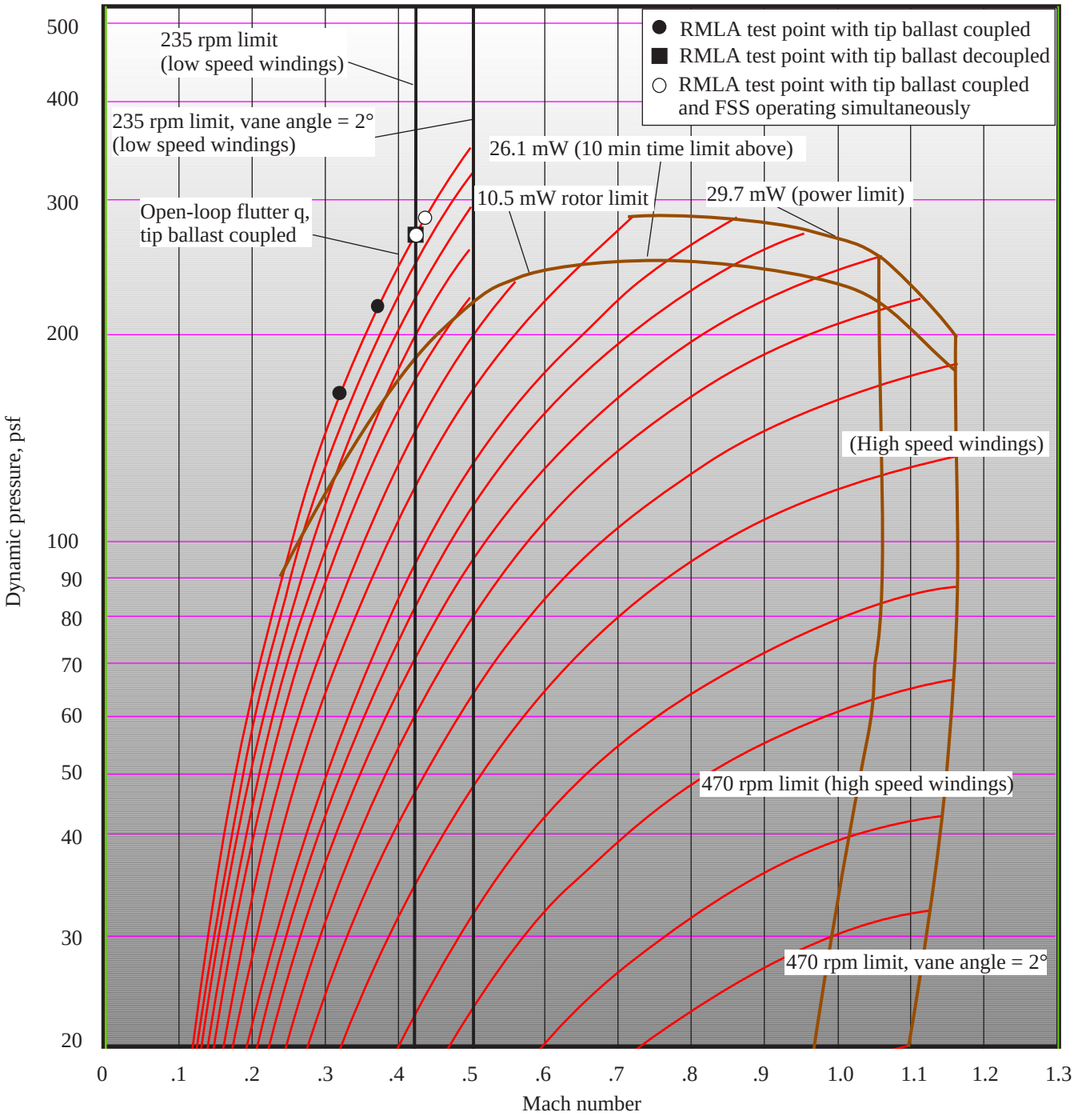

Figure 15. TDT flight envelope in air with RMLA test points identified.

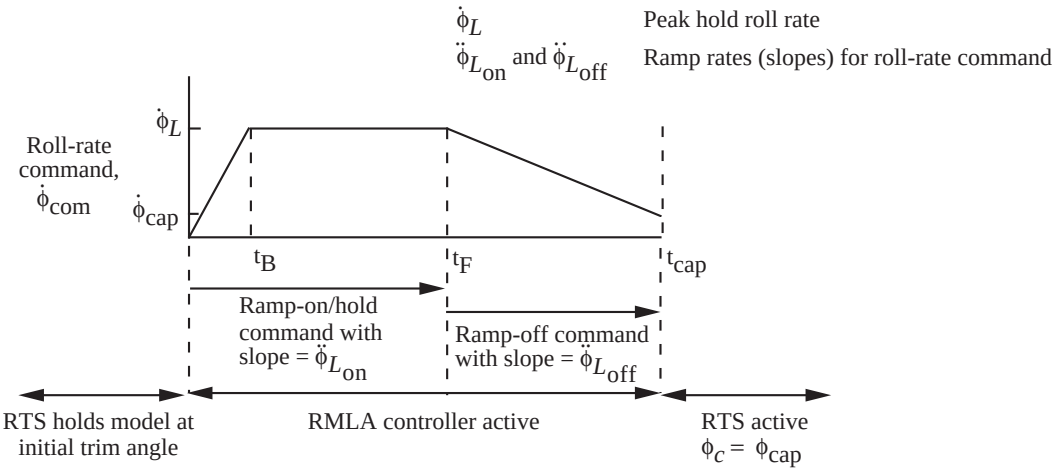

Figure 16. Roll-rate command structure. (From ref. 10.)

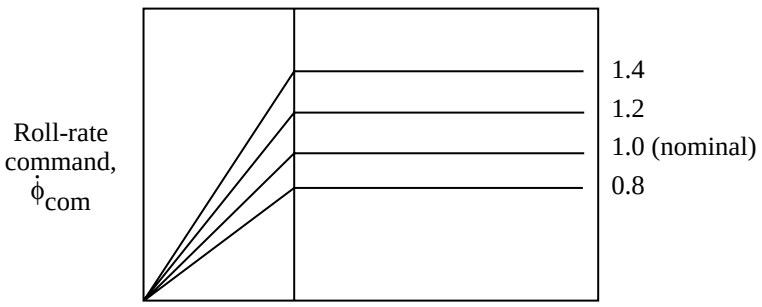

Figure 17. Command input scale factors.

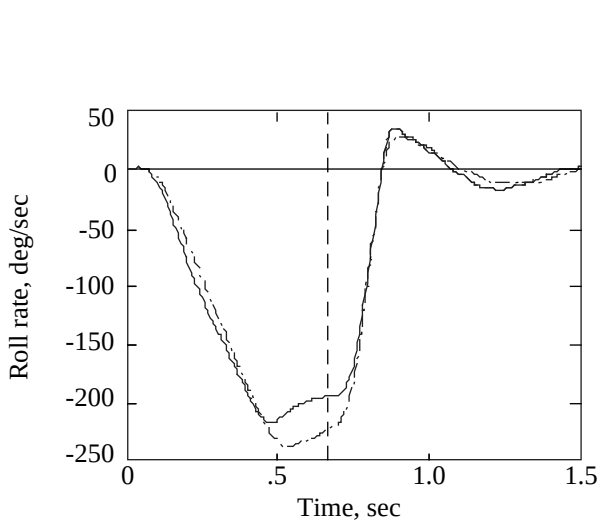

(a) Roll rate.

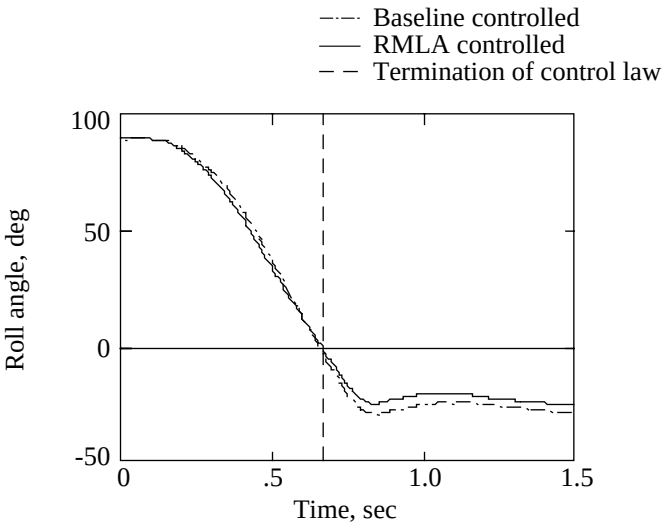

(b) Roll angle.

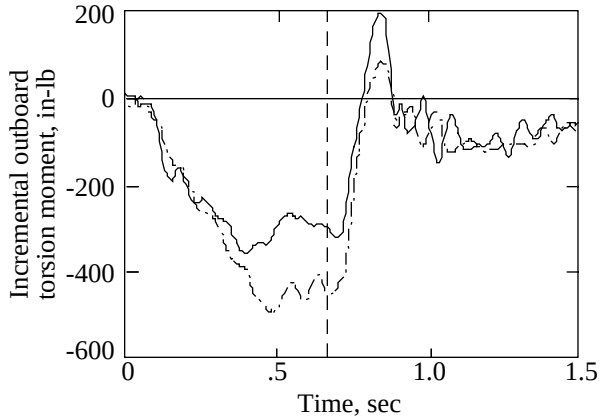

(c) Incremental outboard torsion moment. Peak RMLA = 359.6 in-lb; Peak baseline = 495.1 in-lb.

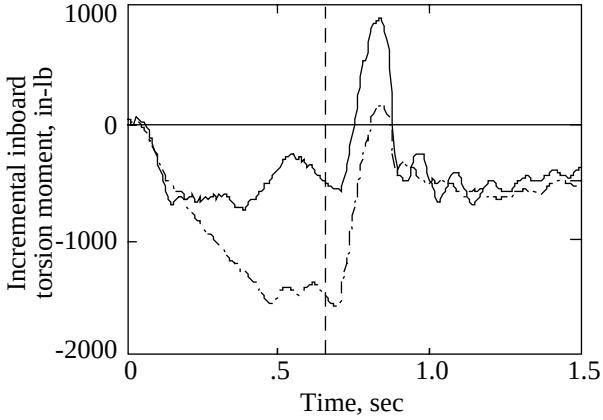

(d) Incremental inboard torsion moment. Peak RMLA = 747.1 in-lb; Peak baseline = 1565.0 in-lb.

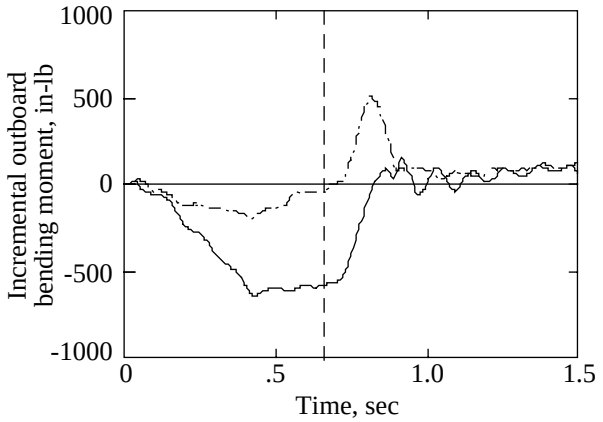

(e) Incremental outboard bending moment. Peak RMLA = 638.0 in-lb; Peak baseline = 185.7 in-lb.

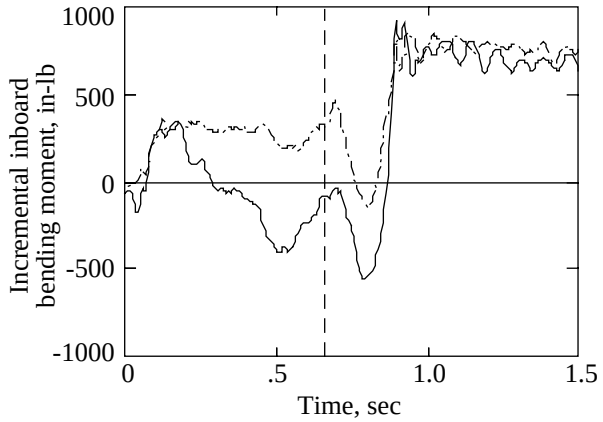

(f) Incremental inboard bending moment. Peak RMLA = 403.8 in-lb; Peak baseline = 352.2 in-lb.

Figure 18. RMLA control law A controlled-maneuver loads compared with baseline loads at $q = 200$ psf.

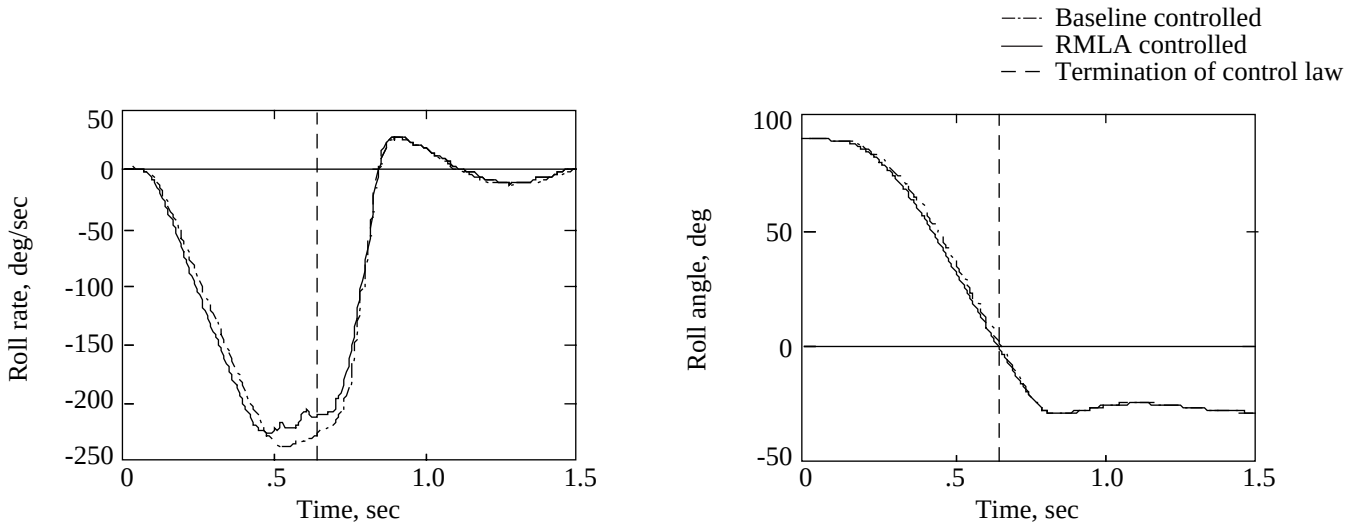

(a) Roll rate.

(b) Roll angle.

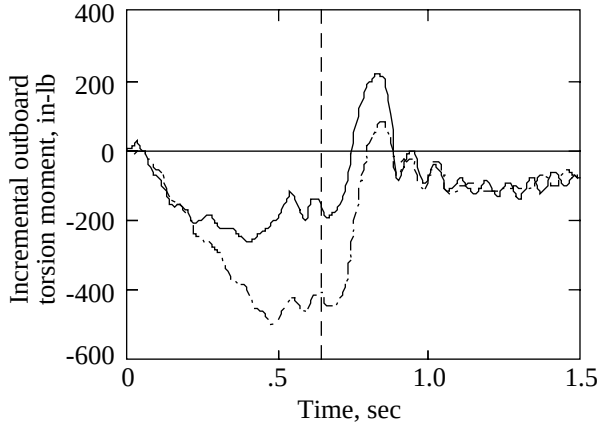

(c) Incremental outboard torsion moment. Peak RMLA = 265.6 in-lb; Peak baseline = 495.1 in-lb.

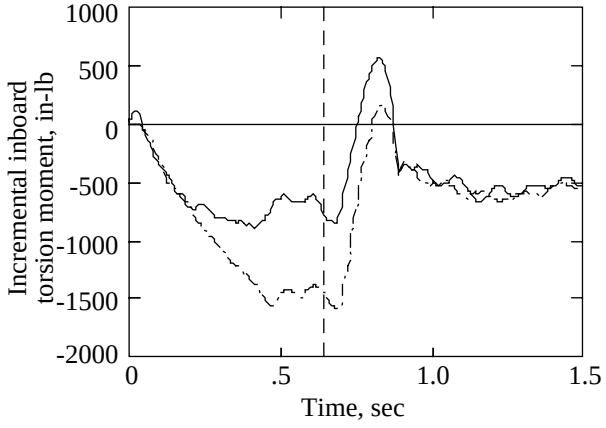

(d) Incremental inboard torsion moment. Peak RMLA = 885.8 in-lb; Peak baseline =1565.0 in-lb.

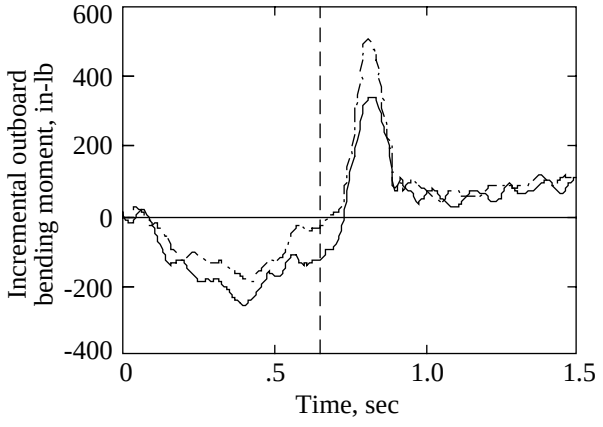

(e) Incremental outboard bending moment. Peak RMLA = 259.5 in-lb; Peak baseline = 185.7 in-lb.

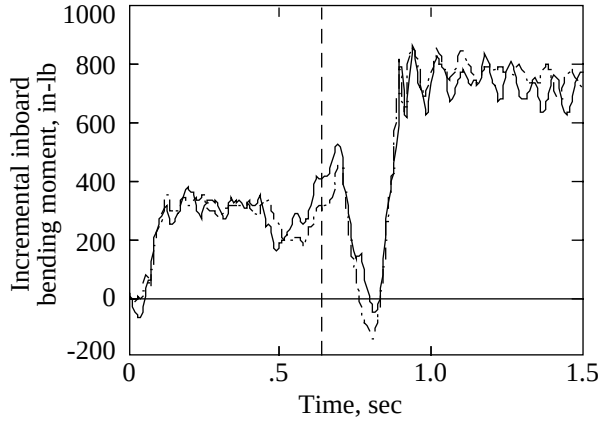

(f) Incremental inboard bending moment. Peak RMLA = 408.6 in-lb; Peak baseline = 352.2 in-lb.

Figure 19. RMLA control law B controlled-maneuver loads compared with baseline loads at $q = 200$ psf.

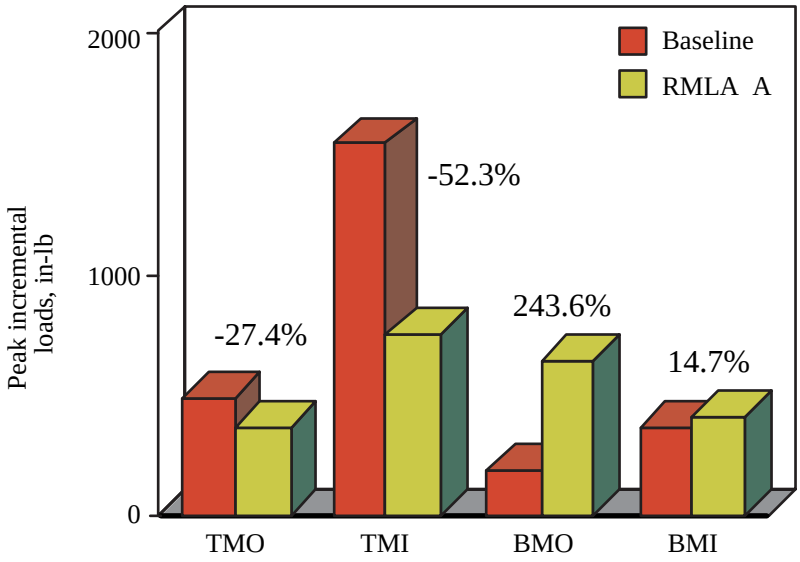

(a) $t_F = 0.66$ sec using control law A.

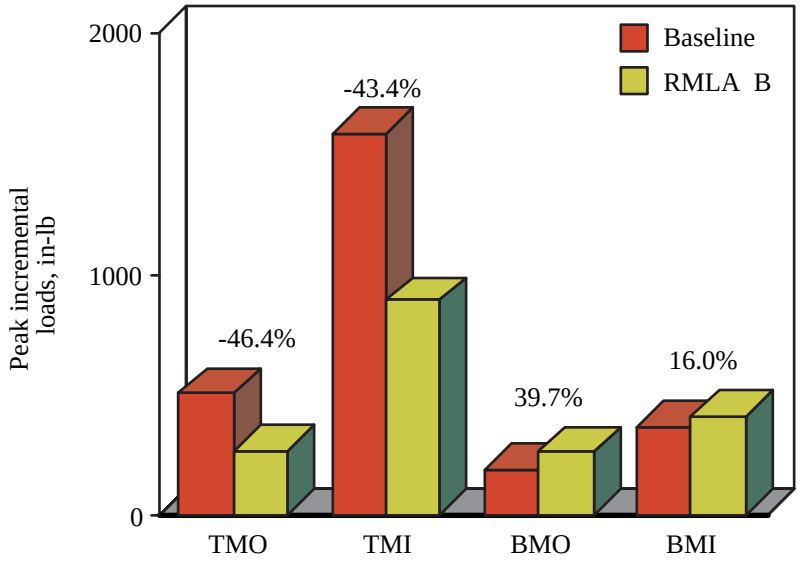

(b) $t_F = 0.645$ sec using control law B.

Figure 20. Change in peak incremental loads for two RMLA-controlled maneuvers with performance times similar to the baseline control law at $q = 200$ psf.

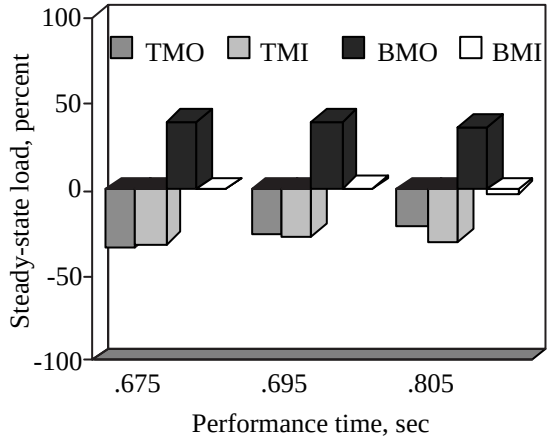

(a) Control law A at $q = 150$ psf.

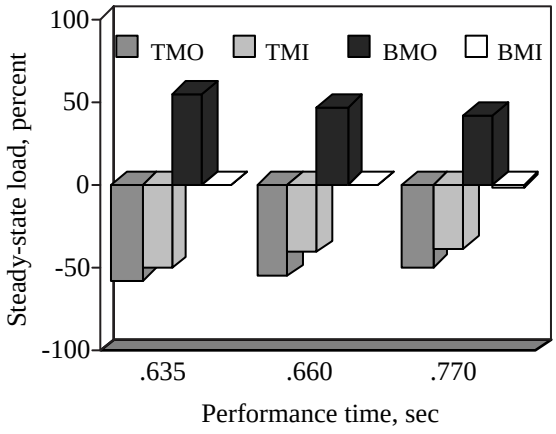

(b) Control law A at $q = 200$ psf.

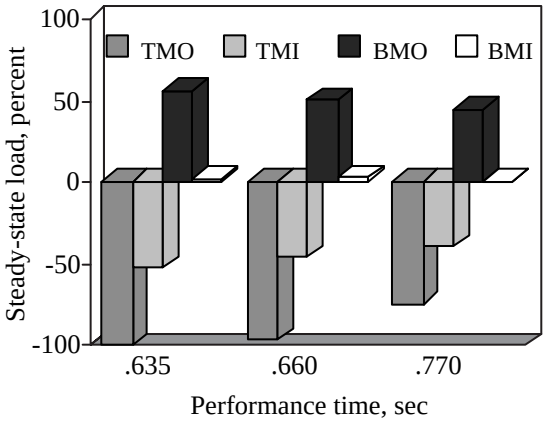

(c) Control law A at $q = 250$ psf.

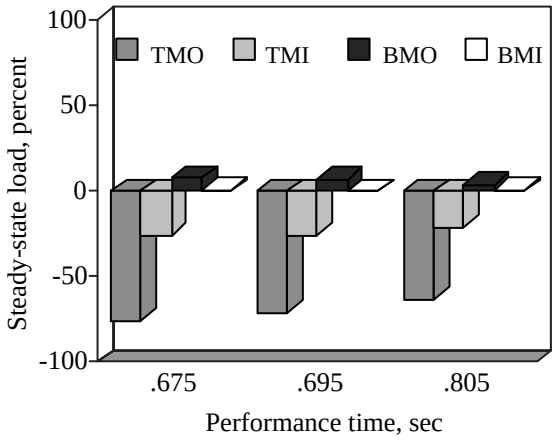

(d) Control law B at $q = 150$ psf.

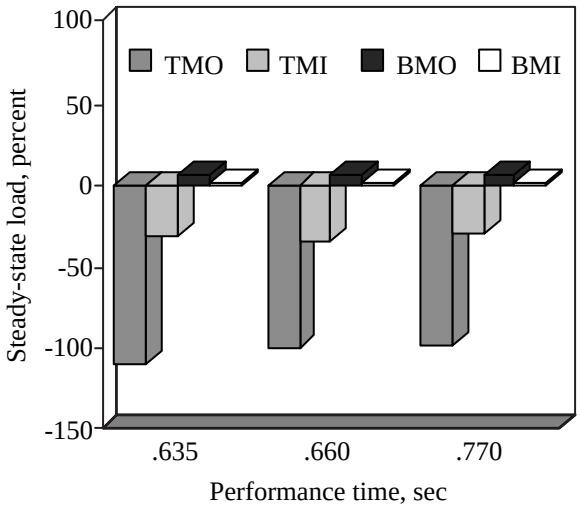

(e) Control law B at $q = 200$ psf.

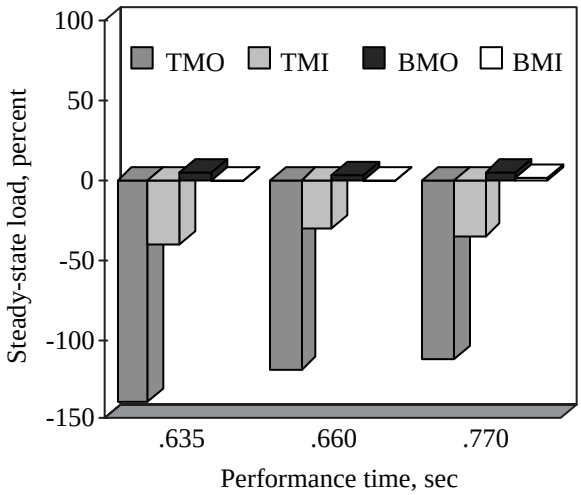

(f) Control law B at $q = 250$ psf.

Figure 21. Percent change in peak incremental load of baseline loads and RMLA-controlled loads relative to steady-state loads at beginning of maneuver.

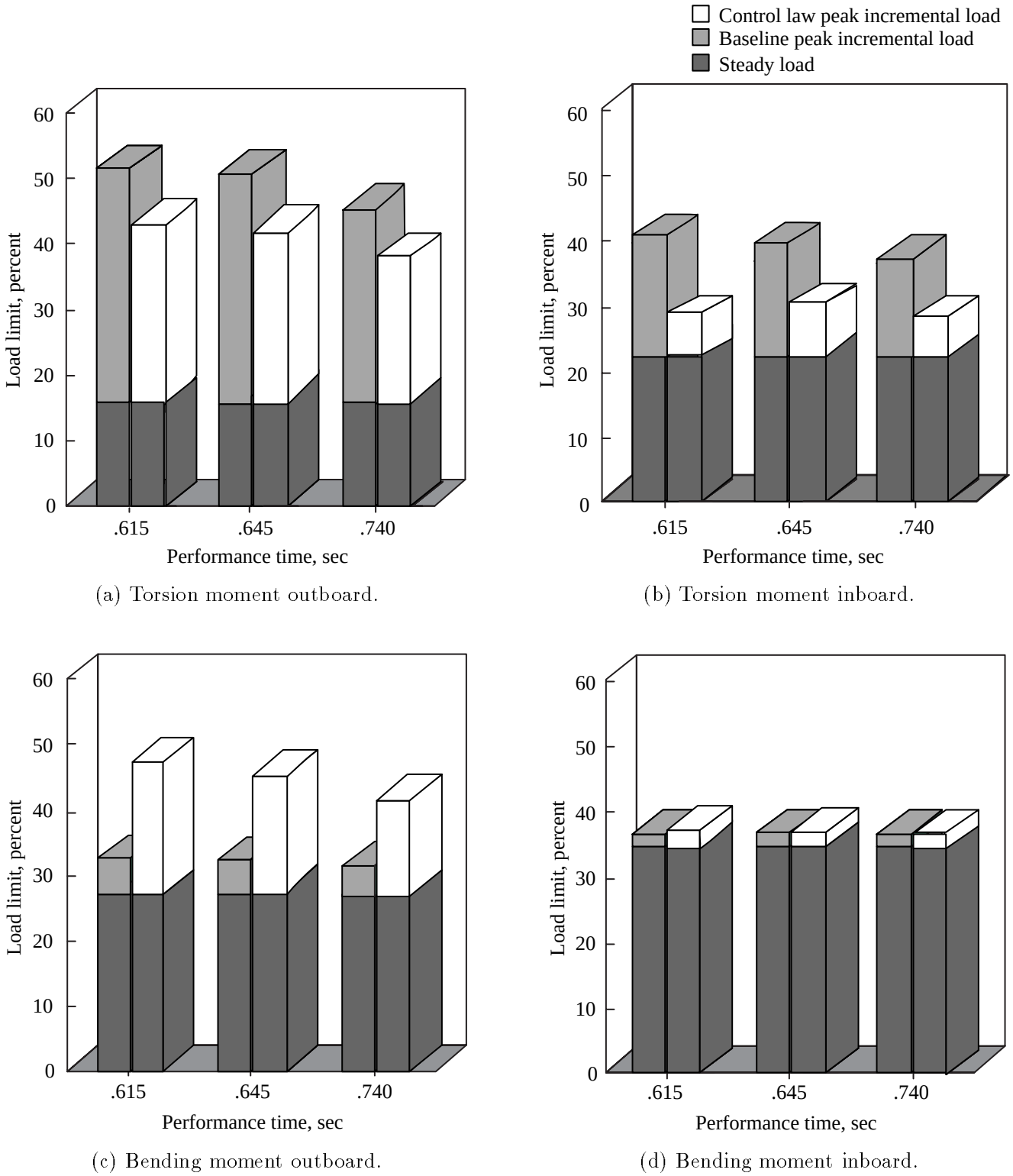

(a) Torsion moment outboard.

(b) Torsion moment inboard.

(c) Bending moment outboard.

(d) Bending moment inboard.

Figure 22. Steady load plus peak incremental relative to static load limits for baseline control law and control law A at $q = 200$ psf.

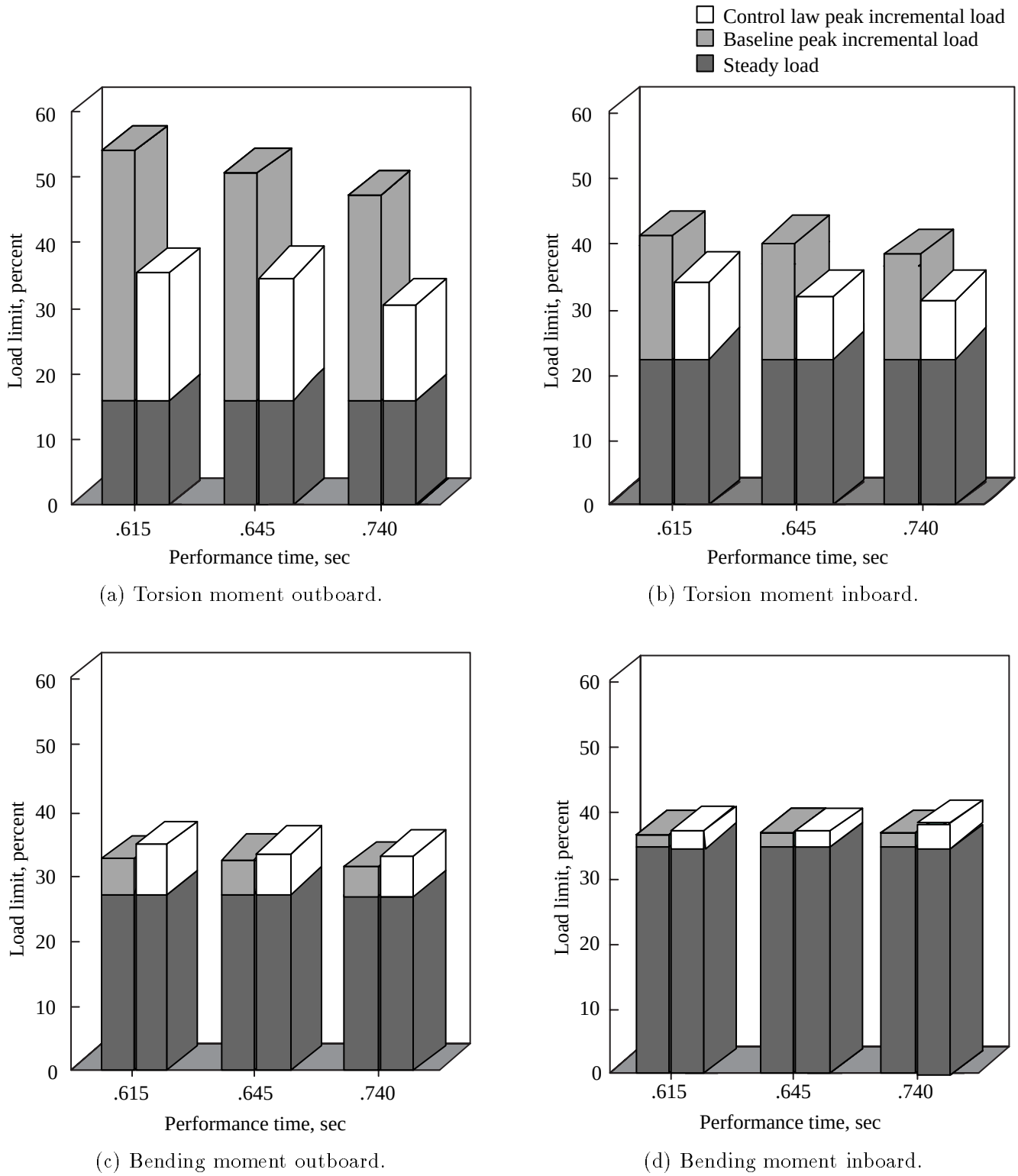

(a) Torsion moment outboard.

(b) Torsion moment inboard.

(c) Bending moment outboard.

(d) Bending moment inboard.

Figure 23. Steady load plus peak incremental relative to static load limits for baseline control law and control law B at $q = 200$ psf.

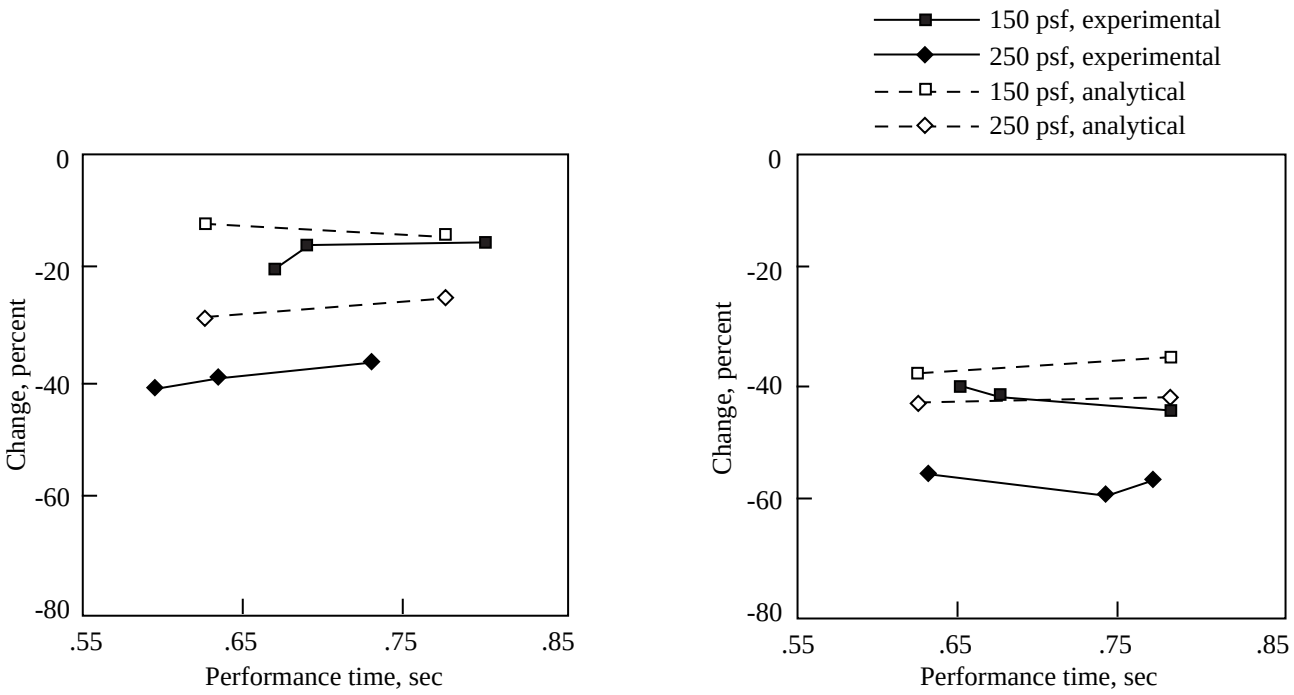

(a) Control law A, torsion moment outboard.

(b) Control law B, torsion moment outboard.

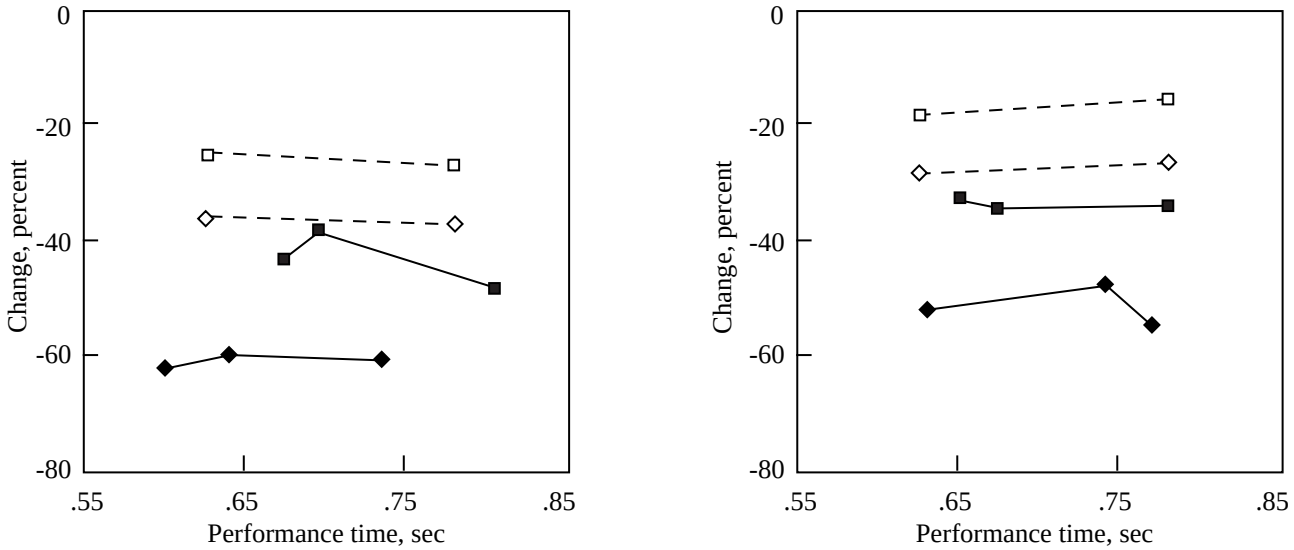

(c) Control law A, torsion moment inboard.

(d) Control law B, torsion moment inboard.

Figure 24. Analytical and experimental incremental load reductions.

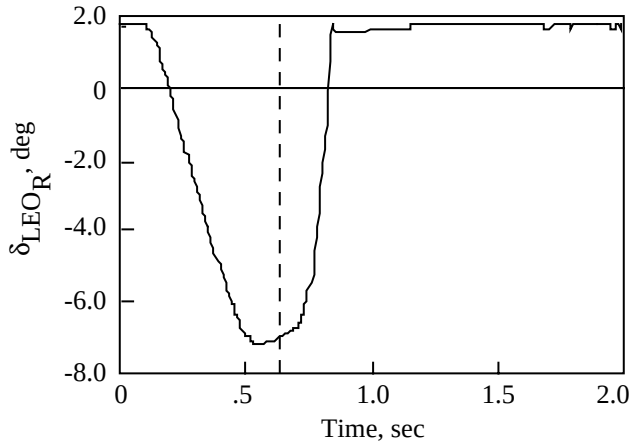

(a) LEO control surface deflection commanded by RMLA control law B.

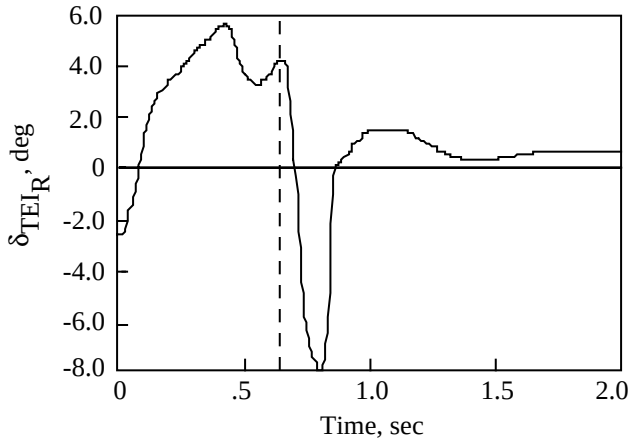

(b) TEI control surface deflection commanded by RMLA control law B.

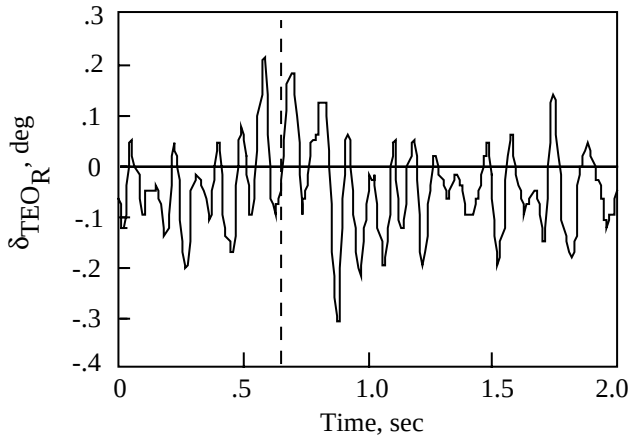

(c) TEO control surface deflection commanded by flutter suppression control law.

Figure 25. Control surface activity during rolling maneuver with simultaneous implementation of RMLA and FSS control laws.

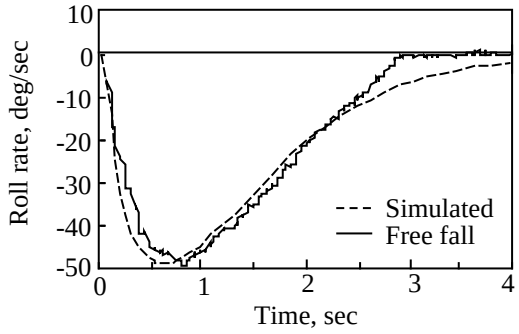

(a) Comparison of simulated roll rate with experimental free-fall roll rate at $q = 150$ psf.

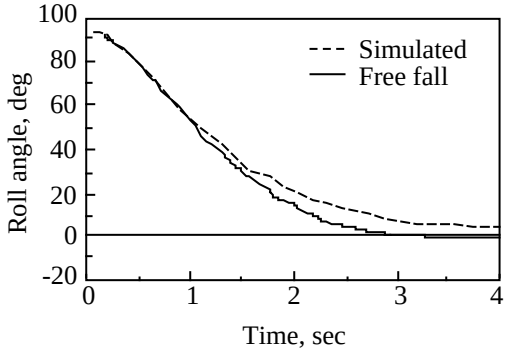

(b) Comparison of simulated roll angle with experimental free-fall roll angle at $q = 150$ psf.

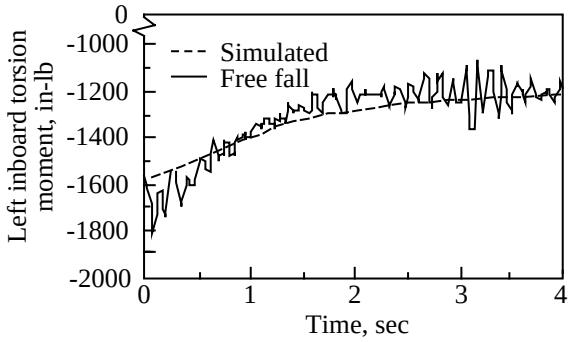

(c) Comparison of simulated left inboard torsion moment with experimental free-fall inboard torsion moment at $q = 150$ psf.

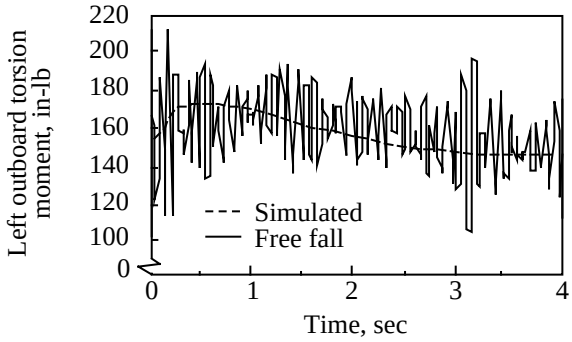

(d) Comparison of simulated left outboard torsion moment with experimental free-fall outboard torsion moment at $q = 150$ psf.

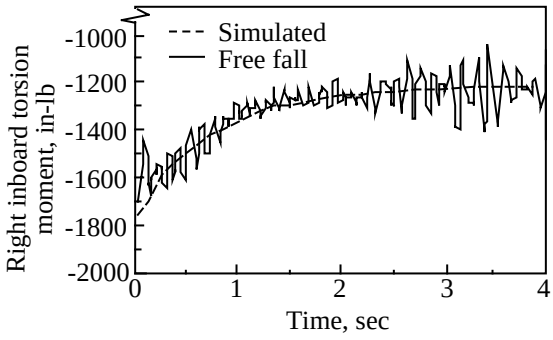

(e) Comparison of simulated right inboard torsion moment with experimental free-fall inboard torsion moment at $q = 150$ psf.

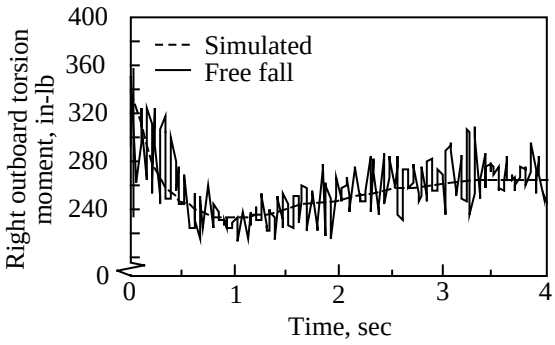

(f) Comparison of simulated right outboard torsion moment with experimental free-fall outboard torsion moment at $q = 150$ psf.

Figure 26. Comparison of simulated and free-fall data.

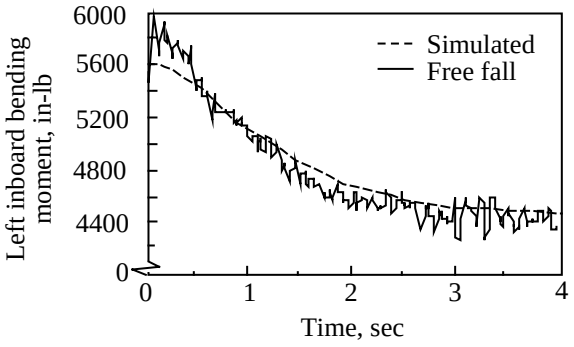

(g) Comparison of simulated left inboard bending moment with experimental free-fall inboard bending moment at $q = 150$ psf.

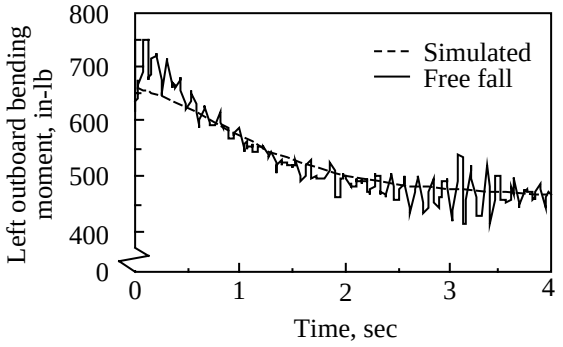

(h) Comparison of simulated left outboard bending moment with experimental free-fall outboard bending moment at $q = 150$ psf.

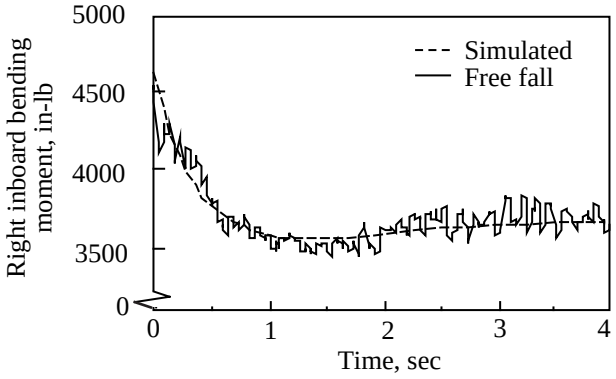

(i) Comparison of simulated right inboard bending moment with experimental free-fall outboard bending moment at $q = 150$ psf.

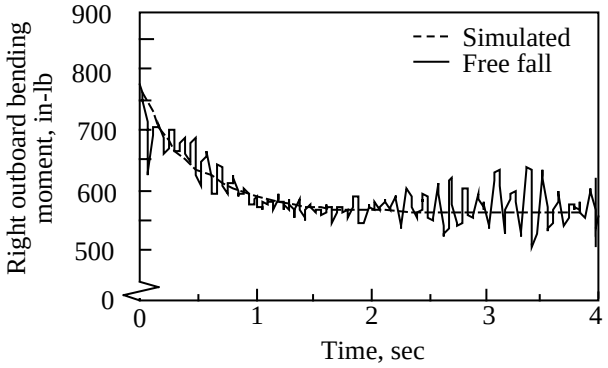

(j) Comparison of simulated right outboard bending moment with experimental free-fall outboard bending moment at $q = 150$ psf.

Figure 26. Concluded.

REPORT DOCUMENTATION PAGE

Form Approved
OMB No. 0704-0188

1. AGENCY USE ONLY *(Leave blank)*	2. REPORT DATE	3. REPORT TYPE AND DATES COVERED
	October 1994	Technical Paper

4. TITLE AND SUBTITLE
Active Load Control During Rolling Maneuvers

5. FUNDING NUMBERS
WU 505-63-36-01

6. AUTHOR(S)
Jessica A. Woods-Vedeler, Anthony S. Pototzky, and Sherwood T. Hoadley

7. PERFORMING ORGANIZATION NAME(S) AND ADDRESS(ES)
NASA Langley Research Center
Hampton, VA 23681-0001

8. PERFORMING ORGANIZATION REPORT NUMBER
L-17053

9. SPONSORING/MONITORING AGENCY NAME(S) AND ADDRESS(ES)
National Aeronautics and Space Administration
Washington, DC 20546-0001

10. SPONSORING/MONITORING AGENCY REPORT NUMBER
NASA TP-3455

11. SUPPLEMENTARY NOTES
Woods-Vedeler and Hoadley: Langley Research Center, Hampton, VA; Pototzky: Lockheed Engineering & Sciences Company, Hampton, VA.

12a. DISTRIBUTION/AVAILABILITY STATEMENT
Unclassified–Unlimited

Subject Category 05

12b. DISTRIBUTION CODE

13. ABSTRACT *(Maximum 200 words)*

A rolling maneuver load alleviation (RMLA) system has been demonstrated on the Active Flexible Wing (AFW) wind tunnel model in the Langley Transonic Dynamics Tunnel (TDT). The objective was to develop a systematic approach for designing active control laws to alleviate wing loads during rolling maneuvers. Two RMLA control laws were developed that utilized outboard control-surface pairs (leading and trailing edge) to counteract the loads and that used inboard trailing-edge control-surface pairs to maintain roll performance. Rolling maneuver load tests were performed in the TDT at several dynamic pressures that included two below and one 11 percent above the open-loop flutter dynamic pressure. The RMLA system was operated simultaneously with an active flutter suppression system above open-loop flutter dynamic pressure. At all dynamic pressures for which baseline results were obtained, torsion-moment loads were reduced for both RMLA control laws. Results for bending-moment load reductions were mixed; however, design equations developed in this study provided conservative estimates of load reduction in all cases.

14. SUBJECT TERMS	15. NUMBER OF PAGES
Aircraft; Rolling maneuver; Wind tunnel; Dynamic loads; Control system	59
	16. PRICE CODE: A04

17. SECURITY CLASSIFICATION OF REPORT	18. SECURITY CLASSIFICATION OF THIS PAGE	19. SECURITY CLASSIFICATION OF ABSTRACT	20. LIMITATION OF ABSTRACT
Unclassified	Unclassified	Unclassified	